Cell Metabolism

Article

Body-wide multi-omic counteraction of aging with GLP-1R agonism

Graphical abstract

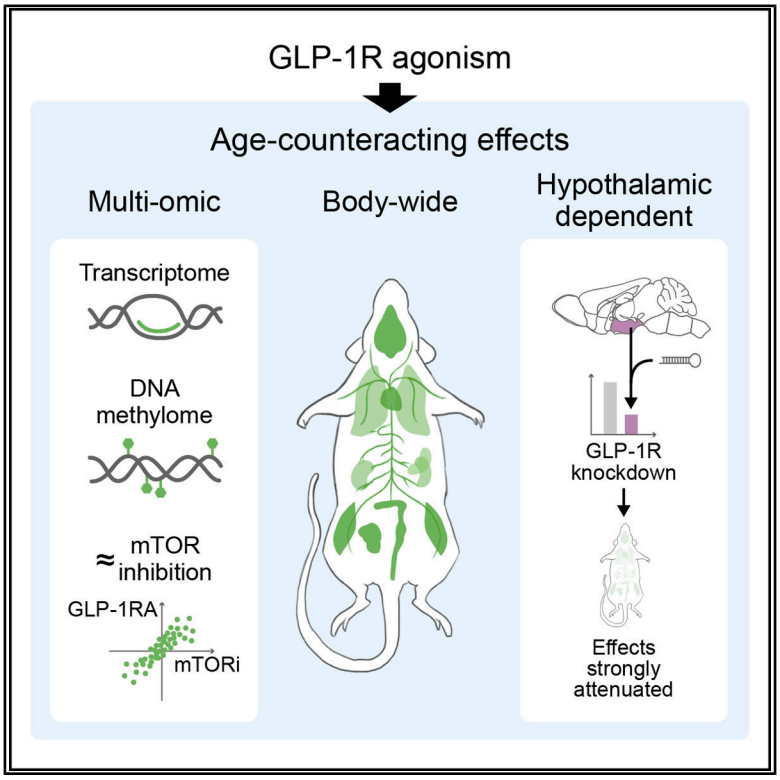

Highlights

- GLP-1R agonist treatment induces multi-omic age-counteraction in male mice
- The molecular age-counteracting effects are dependent on hypothalamic GLP-1R
- Multi-omic impacts closely resemble those of mTOR inhibition

Authors

Junzhe Huang, Andrew J. Kwok, Jason Chak Yan Li, ..., Thomas W. Leung, Vincent C.T. Mok, Ho Ko

Correspondence

junzhe.huang@link.cuhk.edu.hk (J.H.), vctmok@cuhk.edu.hk (V.C.T.M.), ho.ko@cuhk.edu.hk (H.K.)

In brief

GLP-1R agonism counteracts body-wide aging in a brain-dependent manner, mimicking the molecular effects of mTOR inhibition.

Huang et al., 2025, Cell Metabolism *37*, 2362–2380
December 2, 2025 © 2025 The Author(s). Published by Elsevier Inc.
https://doi.org/10.1016/j.cmet.2025.10.014

CellPress

CellPress
OPEN ACCESS

Cell Metabolism

Article

Body-wide multi-omic counteraction of aging with GLP-1R agonism

Junzhe Huang,[1,2,3,4,5,16,*] Andrew J. Kwok,[1,2,3,4,5,16] Jason Chak Yan Li,[1,2,3,4,5,16] Clement Lek Hin Chiu,[1,2,3,4,5,16] Bonaventure Y. Ip,[1,2,3,4,5] Lok Yi Tung,[1,2,3,4,5] Roy C.H. Chan,[1,2,3,4,5] Danny C.W. Chan,[1,2,3,4,5] Ziyu Wang,[1,2,3,4,5] Xianyi Zheng,[1,2,3,4,5] Hoi Tung Chow,[1,2,3,4,5] Michelle P.S. Lo,[1,2,3,4,5] Zhongqi Li,[1,2,3,4,5,6] Nenghan Lin,[1,2,3,4,5] Manyu Wang,[1,2,3,4,5] Leo Y.C. Yan,[1,2,3,4,5] William K.K. Wu,[1,3,7,8] Kim Hei-Man Chow,[1,9] Wei-Jye Lin,[10,11] Yamei Tang,[10,11] Yun Zhang,[12] Weihong Song,[13] Billy Wai-Lung Ng,[1,3,8,14] Sunny H. Wong,[2,15] Thomas W. Leung,[1,2,3] Vincent C.T. Mok,[1,2,3,4,5,*] and Ho Ko[1,2,3,4,5,17,*]

[1]Gerald Choa Neuroscience Institute, The Chinese University of Hong Kong, Shatin, New Territories, Hong Kong SAR, China
[2]Department of Medicine and Therapeutics, Faculty of Medicine, The Chinese University of Hong Kong, Shatin, New Territories, Hong Kong SAR, China
[3]Li Ka Shing Institute of Health Sciences, Faculty of Medicine, The Chinese University of Hong Kong, Shatin, New Territories, Hong Kong SAR, China
[4]Margaret K.L. Cheung Research Centre for Management of Parkinsonism, Faculty of Medicine, The Chinese University of Hong Kong, Shatin, New Territories, Hong Kong SAR, China
[5]Lau Tat-chuen Research Centre of Brain Degenerative Diseases in Chinese, Faculty of Medicine, The Chinese University of Hong Kong, Shatin, New Territories, Hong Kong SAR, China
[6]Department of Neurology, Guangdong Provincial People's Hospital, Guangdong Academy of Medical Sciences, Southern Medical University, Guangzhou, Guangdong Province, China
[7]Department of Anaesthesia and Intensive Care, Faculty of Medicine, The Chinese University of Hong Kong, Shatin, New Territories, Hong Kong SAR, China
[8]Peter Hung Pain Research Institute, Faculty of Medicine, The Chinese University of Hong Kong, Shatin, New Territories, Hong Kong SAR, China
[9]School of Life Sciences, Faculty of Science, The Chinese University of Hong Kong, Shatin, New Territories, Hong Kong SAR, China
[10]Department of Neurology, Guangdong Provincial Key Laboratory of Malignant Tumor Epigenetics and Gene Regulation, Medical Research Center, Sun Yat-Sen Memorial Hospital, Guangzhou, Guangdong Province, China
[11]Guangdong Province Key Laboratory of Brain Function and Disease, Zhongshan School of Medicine, Sun Yat-Sen University, Guangzhou, Guangdong Province, China
[12]Department of Neurology, Nanjing Drum Tower Hospital, Affiliated Hospital of Medical School, Nanjing University, Nanjing, China
[13]Oujiang Laboratory, Center for Geriatric Medicine, The First Affiliated Hospital of Wenzhou Medical University, Wenzhou, Zhejiang Province, China
[14]Guangdong-Hong Kong-Macao Joint Laboratory for New Drug Screening, School of Pharmacy, Faculty of Medicine, The Chinese University of Hong Kong, Shatin, New Territories, Hong Kong SAR, China
[15]Lee Kong Chian School of Medicine, Nanyang Technological University, 11 Mandalay Road, Singapore 308232, Singapore
[16]These authors contributed equally
[17]Lead contact
*Correspondence: junzhe.huang@link.cuhk.edu.hk (J.H.), vctmok@cuhk.edu.hk (V.C.T.M.), ho.ko@cuhk.edu.hk (H.K.)
https://doi.org/10.1016/j.cmet.2025.10.014

SUMMARY

Identifying practical ways to counteract aging and associated degenerative disorders is urgently needed. We performed deep molecular profiling and functional assessments in aging male mice to show that glucagon-like peptide-1 receptor agonist (GLP-1RA) treatment broadly counteracts age-related changes. In mice treated with a GLP-1RA from 11 months for 30 weeks, we observed strong body-wide multi-omic age-counteracting effects and improved selected physical functions. Importantly, the effects were specific to aged mice, not young adults, and were attained with a relatively low dose that minimally affected food intake or body weight. With GLP-1RA treatment beginning at 18 months for 13 weeks, the molecular age-counteracting effects were even stronger and largely dependent on hypothalamic GLP-1R, pointing to a brain-body axis of aging modulation. Comparison with mammalian target of rapamycin (mTOR) inhibition, a proven anti-aging strategy, revealed strong multi-omic similarities. Our findings have broad implications for the mechanisms behind GLP-1RAs' pleiotropic benefits, guiding clinical trials, and informing development of anti-aging-based therapeutics.

 © 2025 The Author(s). Published by Elsevier Inc.
This is an open access article under the CC BY license (http://creativecommons.org/licenses/by/4.0/).

INTRODUCTION

Aging is a complex process involving diverse cellular and molecular alterations across all body systems, resulting in progressive functional decline. Discovering effective strategies to counteract aging-associated changes is a significant scientific pursuit with profound societal implications, given the potential to improve overall well-being and extend healthy lifespan. Numerous strategies have shown promising experimental data, such as mammalian target of rapamycin (mTOR) inhibitors,[1,2] senolytics,[3,4] nicotinamide adenine dinucleotide boosters,[5–7] taurine supplements,[8] intermittent fasting and calorie restriction,[9–11] cellular reprogramming,[12,13] and circulating factor modulation.[14–22] Studies testing these methods have significantly advanced our understanding of the aging process and enhanced our ability to counteract it. An ideal anti-aging method should possess several characteristics, including (1) a pharmacological approach to facilitate practical deployment, (2) a good safety profile with a wide therapeutic window for ease of achieving a good benefit-side effect balance, (3) broad potential applicability to various diseases affecting different organ systems in aging, and (4) potential mechanistic synergy with other therapeutic targets in age-related diseases, allowing for combination therapies. While the above approaches are promising, each has its own set of challenges and limitations. To date, many still require further refinement and development in one or more key attributes for clinical application.[23,24]

Glucagon-like peptide-1 (GLP-1) is a peptide hormone produced by intestinal enteroendocrine cells in the periphery and by preproglucagon-expressing neurons in the brainstem solitary tract nucleus (NTS) in the central nervous system (CNS).[25] In the pancreas, GLP-1 receptor (GLP-1R) signaling enhances postprandial and hyperglycemia-induced insulin release. In the CNS, GLP-1R in the hypothalamus and the brainstem NTS play crucial roles in regulating satiety, metabolism, and other neuroendocrine processes.[25–27] With advancements in understanding GLP-1 biology, multiple GLP-1R agonists (GLP-1RAs) have been developed based on pharmacokinetic innovations and have achieved remarkable success in treating diabetes mellitus (DM) and obesity.[28] Notably, besides cardiovascular and renal benefits,[29–32] GLP-1RA use in DM has shown a wide range of pleiotropic effects, including a reduction in the incidence of cognitive decline,[33,34] Parkinson's disease,[35] and cancers of some organs.[36–38] In non-diabetic overweight or obese subjects, use of GLP-1RA reduced cardiovascular mortality.[39] GLP-1RAs have also demonstrated efficacy in various animal models of neurodegenerative conditions.[40,41] Pilot trials investigating the use of GLP-1RAs in the treatment of non-diabetic patients with dementia[42,43] or Parkinson's disease[44–46] have been conducted, several of which reported encouraging results.[42–45]

We postulate that GLP-1RAs are able to broadly counteract age-related changes body-wide. This would offer a unifying mechanistic explanation for the drugs' effectiveness in diverse disease models and their expanding clinical indications. As a pharmacological approach, GLP-1R agonism also fulfills the above-mentioned criteria for an ideal anti-aging method. We have previously demonstrated that treatment with exenatide (a.k.a. exendin-4, a GLP-1RA) potently counteracts age-related transcriptomic changes across diverse glial and vascular cell types in the mouse brain.[47,48] In this study, we investigate whether GLP-1RA treatment can impart whole-body age-counteracting effects. Such effects, if present, should span across organs, lead to functional improvements, and manifest at several molecular levels, including the transcriptome, DNA methylome, and the circulating metabolome. As GLP-1R is highly expressed by subsets of cells in the hypothalamus,[49] a key regulator of systemic homeostatic processes,[50] we also aim to determine whether the molecular age-counteracting effects depend on CNS GLP-1 signaling through hypothalamic GLP-1R. Finally, we benchmark our GLP-1RA strategy against the mTOR inhibitor rapamycin—currently the most potent pharmacological anti-aging agent.[1]

RESULTS

GLP-1RA treatment improves selected physical functions in aging mice

Past studies have shown that significant molecular changes associated with aging begin to emerge in mice as early as ~10–12 months old,[51–53] accompanied by functional decline.[54–56] We initiated our study in middle-aged mice, which allowed us to capture the early stage of these age-related changes and evaluate the potential preventive effects of GLP-1RA treatment on age-related phenotypes. We first asked whether long-term GLP-1RA treatment could improve physical and cognitive functions. To this end, we administered male C57BL/6 mice with intraperitoneal injection (i.p.) of either a GLP-1RA (exenatide, 5 nmol/kg bw/day, n = 9 animals) or a vehicle (phosphate-buffered saline [PBS], n = 9 animals) for a duration of 30 weeks, starting when the mice were 11 months old, and conducted functional assessments on these animals (Figure 1A). A young control group (n = 10 animals) that received vehicle treatment from 3 months of age for 4 weeks was included for selected comparative analysis (Figure 1A).

To evaluate the impacts on muscle power and motor coordination, we carried out forelimb grip strength and accelerated rotarod tests at baseline, after 3 months, and after 6 months of treatment. Additionally, we employed the Barnes maze and Y-maze, two spatial learning and memory assays, to assess cognitive performance longitudinally (Y-maze) and after 6 months of treatment (Barnes maze). The vehicle-treated mice exhibited significant age-dependent decline in forelimb grip strength (Figure 1B), some apparent decrease in the first 3 months but non-significant overall change in rotarod performance across the 6 months (Figure 1C), and maintained stable performance in the Y-maze measured as novel arm exploration time proportion across ages (Figure S1A). The exenatide-treated mice demonstrated enhancements in both forelimb grip strength (Figures 1B and 1D) and rotarod test performances (Figures 1C and 1E) relative to the vehicle group animals of the same age and treatment duration. The effects became progressively more pronounced over the 6-month treatment period (Figures 1D and 1E). Consistent with the lack of age-related decline observed in the Y-maze performance in the vehicle group, exenatide treatment only exhibited a trend of improving the performance in this assay based on trend test, but not when directly comparing the treatment endpoint data

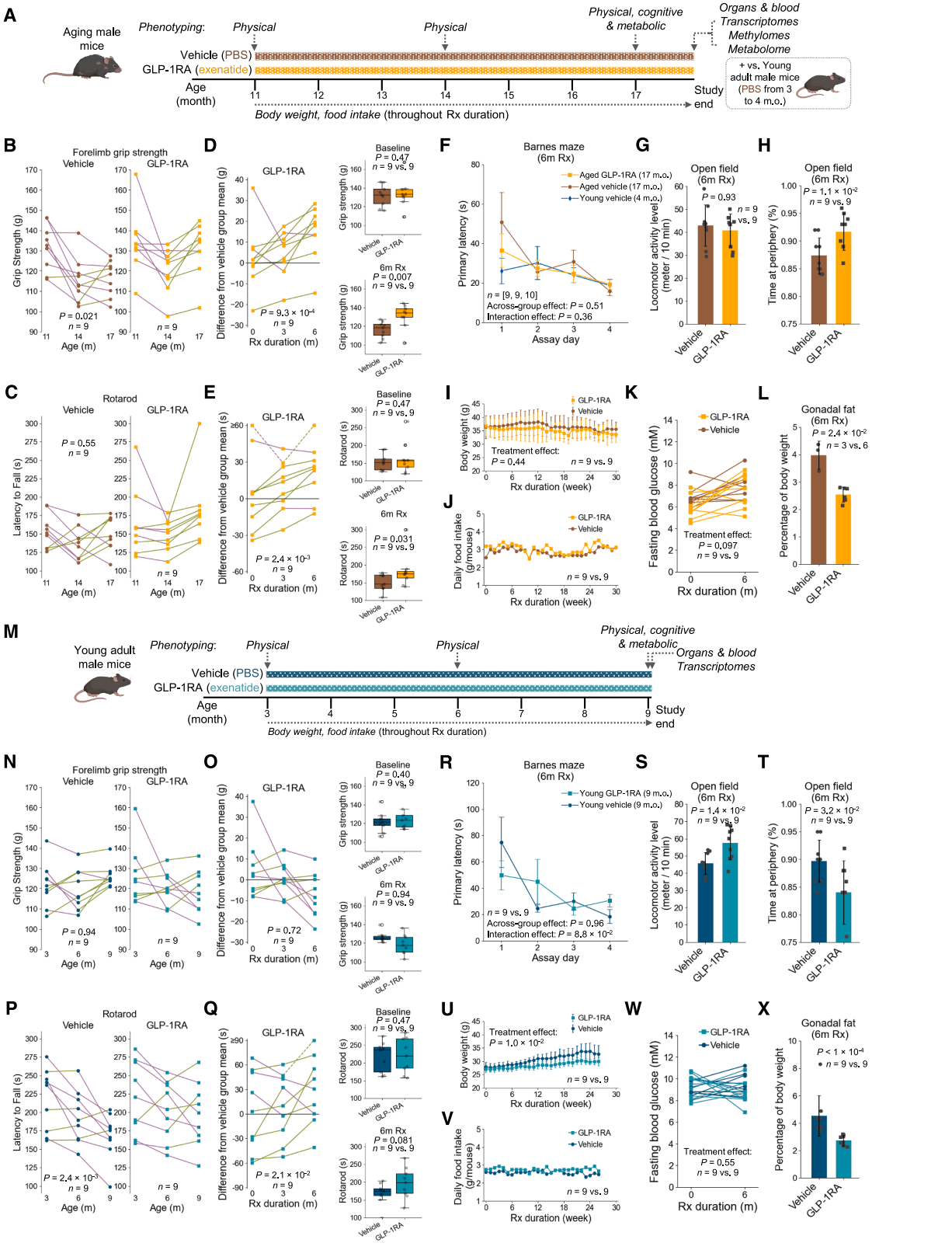

(legend on next page)

(Figure S1B). In the Barnes maze test, we did not observe significant differences in primary latency to reach the target between the experimental groups (Figure 1F). Although assay day 1 data showed that aged vehicle-treated mice on average tended to take longer to find the target than the young vehicle-treated control group, with the aged exenatide group's performance in between, the performance across all groups converged from assay day 2 onward (Figure 1F). Number of errors made on assay days 1–4, and performances in probe trials also exhibited no significant differences across groups (Figure S1C).

We further assessed exploratory and anxiety-like behaviors using the open-field test after 6 months of treatment. Total locomotor activity did not differ between exenatide- and vehicle-treated mice (Figure 1G). However, exenatide-treated mice spent significantly more time in the periphery of the behavioral arena compared with vehicle controls (Figure 1H), indicating increased center avoidance. Notably, a previous study reported that aging alters anxiety-like behavior in male mice, including decreased center avoidance in open-field test.[54] Additionally, we employed a machine vision-based algorithm to calculate a frailty index (FI) score from open-field video recordings.[57] In our dataset, the algorithm-predicted FI demonstrated a clear increase when comparing middle-aged (9 months old) with young (4 months old) mice (Figure S1E). When examining the FI progression from middle age to older age (17 months old), only two of four prediction models detected non-significant upward trends, while the other two showed no further increase (Figure S1E), demonstrating less pronounced predicted FI differences over this age range, consistent with the original study.[57] Upon completion of 6-month treatment, comparisons between exenatide and vehicle treatment groups revealed no differences in the algorithmically determined FI in the aged mice (Figure S1F).

To control for potential confounding factors that could impact aging, we closely monitored body weight and food intake throughout the treatment period, while fasting blood glucose was also assessed after 6-month treatment. Importantly, at the chosen dosage of exenatide, there were no significant differences in body weight (Figure 1I) or food intake (Figure 1J) between the two groups during the treatment period. We further established that the functional benefits observed were not confounded by body weight loss. Specifically, linear model fitting showed that body weight change did not significantly influence the relative improvements in forelimb grip strength or rotarod performance, yielding non-significant positive coefficients (Figures S1G and S1H). This was corroborated by correlation analysis, which also revealed no negative relationship between weight change and the functional readouts after 3 or 6 months of exenatide treatment (Figures S1G and S1H). Additionally, there were no observed differences in fasting blood glucose levels between the two groups after 6 months of treatment (Figure 1K). The exenatide-treated group exhibited a reduction in gonadal fat as a percentage of body weight (Figure 1L), which aligns with the known pharmacological action of GLP-1RAs.[58]

We also carried out a separate set of experiments in young male mice (n = 9 animals each group), starting at 3 months old (Figure 1M). In contrast to the aged mice, the young mice treated with exenatide did not perform better in the forelimb grip strength test (Figures 1N and 1O), yet they exhibited a marginal improvement in the rotarod test relative to the vehicle group (Figures 1P and 1Q), which declined with age from 3 to 9 months old (Figure 1P). Exenatide-treated young mice did not outperform the vehicle-treated counterparts in Barnes maze (Figures 1R and S1D) and displayed a slight increase in overall locomotion in the open-field test (Figure 1S), along with increased time spent at the center (Figure 1T) after 6 months of treatment. Exenatide

Figure 1. Physical, cognitive, and metabolic readouts in two cohorts of male mice: Aging mice treated with a GLP-1RA (exenatide) or vehicle for 30 weeks starting at 11 months old and young adult mice for 26 weeks starting at 3 months old

(A) Schematic of experimental design for the cohort of aging mice with long-term treatment.

(B and C) Performances of aging mice treated with exenatide vs. phosphate-buffered saline (PBS) vehicle in forelimb grip strength and accelerated rotarod tests across ages. Raw values are plotted.

(D and E) Left: forelimb grip strength and rotarod performances of aging mice treated with exenatide plotted as differences from vehicle group mean at each treatment duration time point. Right: boxplots comparing the respective performance measures at baseline or after 6-month treatment.

In (B)–(E), dots connected by lines are longitudinal data from individual animal subjects, and the lines are color-coded according to temporal change across two consecutive time points of assessment (green: increase; magenta: decrease). Dashed lines in the left of (E) indicate lines connecting to dots with values beyond the y axis upper limit.

(F) Performances of the exenatide- and vehicle-treated aging mice in the Barnes maze test after 6-month treatments (i.e., tested at 17 months old), and that of a group of young adult male mice after 4-week vehicle treatment (at 4 months old). Mean (±SEM) of primary latencies to reach target over four consecutive assay days are shown for each experimental group. Each mouse was tested once on assay day 1 (after the initial training trial), and twice daily on assay days 2–4. Primary latencies were averaged to obtain the value for each day on assay days 2–4. Shorter primary latencies indicate better performances. Sample sizes are indicated in squared brackets (numbers of animals for aged GLP-1RA, aged vehicle, and young vehicle groups).

(G and H) Bar plots (mean [±SD]) of open-field test behavioral readouts, including locomotor activity level measured as total travel distance over 10 min and proportion of time spent at the periphery (reflecting anxiety-like behavior) for the two aging treatment groups after 6-month treatments.

(I) Mean (±SD) body weights of the two aging animal groups throughout the treatment period (monitored weekly).

(J) Average daily food intake per mouse for the two aging animal groups throughout the treatment period (monitored weekly).

(K) Fasting blood glucose levels at baseline and after 6-month treatments for each animal subject in the two aging treatment groups.

(L) Gonadal fat weight as percentage of body weight in the two aging treatment groups.

(M–X) Similar to (A)–(L), but for the cohort of young adult mice with long-term treatment. Note that for this cohort, mice were tested once daily in Barnes maze at 9 months old.

Sample sizes: n = 9 mice (biological replicates) for each experimental group, except n = 10 4-month-old biological replicates that received vehicle treatment, for data presented in (B)–(K) and (N)–(X). n = 3 and 6 biological replicates for exenatide and vehicle treatment groups, respectively, for data presented in (L). These apply to the statistical tests in the respective panels. p values: (B, C, N, and P, left) Page's trend test for decreasing trend; (D, E, O, and Q, left) Page's trend test for increasing trend; right, one-sided rank-sum test (to examine if exenatide group > vehicle group values); (F) two-way mixed ANOVA; (G, H, L, S, T, and X) two-sided rank-sum test; (I, K, R, U, and W) two-way repeated-measures ANOVA. Rx, treatment.

reduced body weight gain in the young mice (Figure 1U), despite their food intake remaining unaffected (Figure 1V). Similar to the aged animals, there were no observed differences in fasting blood glucose between the two groups after 6 months of treatment (Figure 1W), whereas gonadal fat was also reduced by the long-term exenatide treatment (Figure 1X).

Collectively, these results revealed a consistent pattern whereby GLP-1RA treatment most effectively benefits physiological functions that exhibit more prominent age-related decline, including forelimb grip strength and rotarod performance. By contrast, measures that remained more stable across the period of treatment did not show significant improvement (e.g., Y-maze performance, Barnes maze learning, and FI), although we do not rule out the possibility that larger mouse cohorts may reveal more subtle differences. This observation was further reinforced by the minimal exenatide treatment effects in the younger mice, where age-related declines had largely not yet occurred. These findings suggest that GLP-1RA treatment may selectively target aging-vulnerable pathways rather than indiscriminately enhancing all functions.

GLP-1R agonism ameliorates body-wide age-related molecular changes across multiple omic levels

We next aimed to explore whether the observed functional benefits were associated with the counteraction of age-related molecular changes. To this end, at the conclusion of the treatment period we collected various tissue organs and blood samples from the animals for multi-omic assessments (Figure 1A). We included a young male mouse group that received vehicle treatment for differential analyses (Figure 1A).

Using bulk RNA sequencing, we compared the age-related and exenatide treatment-induced transcriptomic changes throughout the body. Strikingly, exenatide treatment led to a widespread counteraction of age-related transcript expression changes in numerous tissue organs, as well as in circulating white blood cells (WBCs) (Figures 2A–2H and S2A–S2E). This effect was particularly prominent in metabolically demanding tissues and organs, including the brain regions hypothalamus and frontal cortex (Figures 2A and 2B), gonadal adipose tissue (Figure 2C), colon (Figure 2D), heart (Figure 2F), and skeletal muscle (Figure 2G). Based on sensitivity analysis involving random permutation of aged mouse treatment group labels (STAR Methods), the transcriptomic age-counteraction was the most robust in the hypothalamus, frontal cortex, adipose tissue, colon, circulating WBCs, heart, and skeletal muscle (Figures S3A and S3B). The age-counteracting effect of exenatide was also evident on principal component analysis (PCA) of gene expression patterns in various tissue organs. Despite some sample-to-sample variance inherent to transcriptomic profiling across animals and age, for the hypothalamus, frontal cortex, adipose tissue, colon, and circulating WBCs, the overall distribution and centroid of the aged exenatide group data points shifted away from the aged vehicle group and toward the young vehicle group (Figure S4A). The age-related transcriptomic changes that were counteracted by exenatide treatment varied across the different tissue organs and circulating WBCs (Figures 2A–2G, right), consistent with the known organ-specific patterns of aging-associated expression changes.[51] Additionally, exenatide treatment counteracted age-related metabolomic changes in the circulation (Figure 2I), apart from the effect observed in the circulating WBC transcriptome (Figure 2E). Many functionally relevant genes, including those associated with key hallmarks of aging,[59,60] such as cellular senescence (Figure 3A), oxidative phosphorylation (Figure 3B), and macroautophagy (Figure 3C), exhibited predominantly opposite patterns of transcript expression level changes between aging and exenatide treatment across the tissue organs and circulating WBCs. Enrichment analysis on the age-related transcript expression changes counteracted by exenatide treatment implicated diverse impacts on organ/tissue-specific functions, as well as shared processes across body sites (Figures 3D and S2F).

To further examine transcriptomic changes holistically, we performed weighted gene co-expression network analysis[61] (WGCNA), identifying differentially expressed gene modules across the tissue organs in aging (Figure 3E), which were expectedly enriched with genes associated with various aging-associated cellular processes (Figure S4B). Notably, exenatide treatment predominantly modulated gene module expression in a manner counteractive to aging across tissue organs and circulating WBCs (Figure 3E). Many exenatide treatment-induced differentially expressed modules were enriched in genes involved in biological processes that undergo age-dependent changes (Figures 3F and 3G). Exenatide-upregulated modules most counteractive to aging (adipose tissue modules 3, 8, 9; circulating WBCs module 1; colon module 2; frontal cortex module 10; hypothalamus modules 2, 9; spleen module 15) showed significant enrichment in protein translation/proteostasis, senescence, inflammatory response, and lysosome/autophagy/mitophagy pathways (Figures 3E and 3F). Modules that were downregulated by exenatide treatment and counteractive to aging (adipose tissue module 4; colon modules 1, 33; frontal cortex module 14; hypothalamus module 1; kidney module 12; lung module 17; skeletal muscle modules 8, 16) were enriched in similar functional pathways (Figures 3E and 3G). These further indicated that exenatide counteracts aging-associated and functionally relevant transcriptional changes across the tissue organs.

Epigenetic changes play a crucial role in regulating gene expression and are recognized as a hallmark of aging.[59,60] We further investigated the effects of GLP-1RA treatment on DNA methylation (DNAm) patterns and their correlation with age-related modifications using a DNA microarray that covers over 320,000 CpG sites.[62,63] These consist of ~285,000 mouse CpG sites,[64] and it also allows imputation of ~40,000 sites conserved among multiple mammalian species, the effects on which may have higher generalizability across species.[62,63] We first analyzed the treatment impact on the ~285,000 mouse sites. Similar to the transcriptomic level, we found that exenatide treatment effectively and broadly counteracted aging-associated methylation changes across multiple tissues, encompassing brain regions (the hypothalamus, frontal cortex, and hippocampus), gonadal adipose tissue, circulating WBCs, heart, and skeletal muscle (Figures 4A and 4B). Interestingly, the age-counteracting effect was not evident on the colon or spleen methylome (Figures 4A and 4B), despite the transcriptomic age-counteraction in the colon (Figures 2D and 2H). By contrast, exenatide treatment-induced methylation changes antagonistic to those that occurred in aging in the kidney and liver

CellPress
OPEN ACCESS

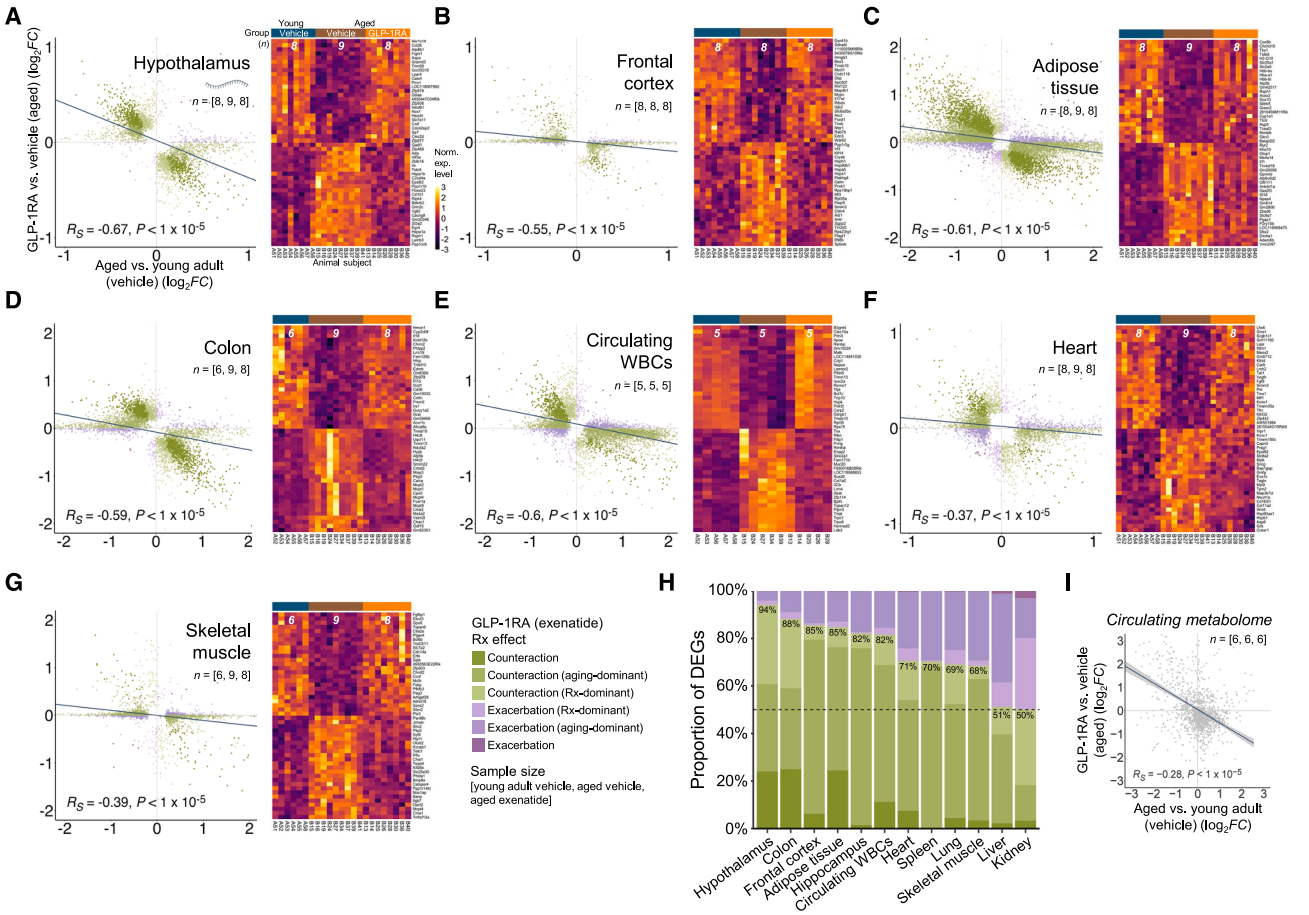

Figure 2. Transcriptomic impacts across tissue organs and circulating WBCs in aging male mice treated with a GLP-1RA (exenatide) for 30 weeks starting at 11 months old and associated circulating metabolomic changes

(A–G) Left: scatterplots showing transcriptomic changes in aging (*x* axis) vs. exenatide treatment (*y* axis) in different tissue organs and circulating WBCs. Each dot represents one differentially expressed gene (DEG), color-coded by treatment (Rx) effect categories as shown in the inset (counteraction, opposing aging and Rx effects; exacerbation, same aging and Rx effects; aging- or Rx-dominant, statistically significant in the respective comparison only; no additional label, significant for both aging and Rx effect comparisons; see also STAR Methods). Inset of (A): symbol for transcript. Right: heatmaps of the expression levels of top 50 protein-coding genes with aging-associated differential expressions that were counteracted by exenatide treatment (25 upregulated and 25 downregulated) in the different tissue organs and circulating WBCs (see STAR Methods for ranking methodology).

(H) Summary bar plot of the proportions of DEGs under the different Rx effect categories (as specified in the inset of A–G).

(I) Scatterplot showing plasma metabolomic changes in aging (*x* axis) vs. exenatide treatment (*y* axis). Each dot represents one metabolite.

In (A)–(G) and (I), the lines represent linear fits (with confidence interval [gray] in I). The Spearman correlation coefficients (R_S) and associated *p* values are also shown. Numbers in squared brackets for each scatterplot and at the top of each heatmap indicate sample sizes for each profiling (numbers of mice [biological replicates] for young adult vehicle, aged vehicle, and aged exenatide groups).

(Figures 4A and 4B), whereas we did not detect dominant transcriptomic age-counteracting effects for these organs (Figures 2H, S2D, and S2E). In sensitivity analysis with permutation of aged mouse treatment group labels (STAR Methods), the phenomenon was the most robust in the hypothalamus, frontal cortex, adipose tissue, and heart (Figures S3C and S3D). We obtained similar results with additional analysis focusing on the ~40,000 imputed multi-mammalian conserved sites (Figures 4C and S5A). We also further analyzed two established DNAm age clocks,[63,65] yet we did not observe statistically significant reductions in epigenetic age clocks in any tissues after exenatide treatment (Figure S5B).

For the young male mouse cohort (Figure 1M), we similarly profiled transcript expression changes across tissues and organs and compared the exenatide treatment-induced differential expressions with those found in the aged animals (Figure S6). Generally, exenatide treatment resulted in fewer and distinct expression changes in the young cohort. This was reflected by the much smaller numbers of significantly differentially expressed genes caused by exenatide treatment and the lack of correlation in exenatide induced differential expression between young and aged animals (Figure S6), except for circulating WBCs, where a modest positive correlation was observed (Figure S6). These indicate that the age-counteracting transcriptomic effects of GLP-1RA treatment are largely specific to the aged mouse.

Taken together, these findings provided compelling evidence that the functional benefits observed in aged mice following

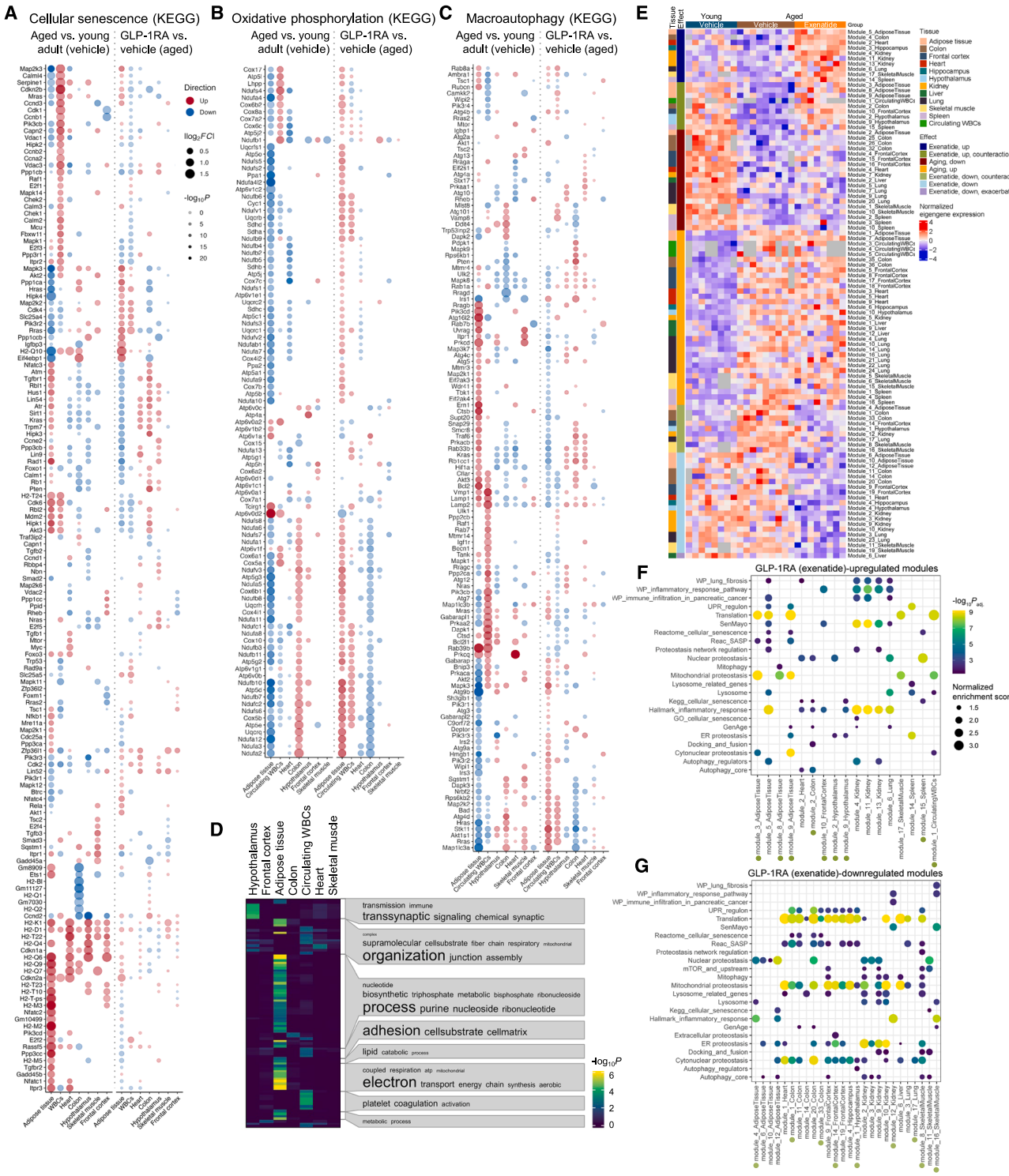

Figure 3. Transcriptomic impacts across tissue organs and circulating WBCs in aging male mice treated with a GLP-1RA (exenatide) for 30 weeks starting at 11 months old

(A–C) Dot plots showing differentially expressed genes (DEGs) annotated with three aging-associated functional pathways in the Kyoto Encyclopedia of Genes and Genomes (KEGG) database, namely cellular senescence, oxidative phosphorylation, and macroautophagy. A gene is featured if it exhibits significant differential expression in at least one comparison (i.e., aging and/or treatment effects). For each featured gene, its differential expression is visualized with dots in plots corresponding to both the aging and treatment effects within the gene panel.

(legend continued on next page)

long-term GLP-1RA treatment are closely linked to counteraction of aging at the transcriptomic, epigenetic, and metabolomic levels in body-wide tissue organs.

GLP-1RA age-counteracting molecular effects are partially mediated via a hypothalamic receptor-dependent brain-body axis

The functional and multi-omic age-counteracting effects of GLP-1RA treatment can in theory be mediated by systemic impacts driven by GLP-1R activation in the CNS, the pancreas, and/or local actions at different body sites. Although it is difficult to completely separate and quantify the relative contributions of each component in every tissue organ, we recognized the importance of gaining a better understanding of the mechanisms involved in the age-counteracting effects of GLP-1RA treatment. To address this, we sought to investigate the potential role of hypothalamic GLP-1R in the age-counteracting molecular effects of GLP-1RA treatment.

We performed experiments using separate groups of male mice at an older age than the previous batch, starting treatments at 18 months old and continued for 13 weeks (i.e., ~3 months) (Figure 5A). These mice were divided into different groups: one group received a hypothalamic adeno-associated virus vector (AAV) injection to express a short hairpin RNA (shRNA) and specifically knockdown *Glp1r* in the hypothalamus, while another group received a control AAV injection with a scramble shRNA (Figure 5A). Both groups were further divided into subgroups that either received exenatide treatment (at the same dose as before) or PBS vehicle (Figure 5A) (n = 5 male mice for each of the aged experimental subgroups; see also Table S1). Additionally, a young adult vehicle control group (n = 6 male mice) that received scramble shRNA AAV injection was included for comparisons (Figure 5A). From a subset of animals from each of the experimental groups or subgroups (n = 3 mice per group/subgroup), we assayed *Glp1r* transcript abundance in the hypothalamus with quantitative PCR (STAR Methods) and observed a reduction of near or over 50% in the knockdown subgroups (Figure 5B). We also validated our receptor knockdown protocol at the protein level with immunohistochemistry, noting strong attenuation of hypothalamic GLP-1R staining signals in the dorsomedial, ventromedial, and arcuate nuclei (Figures S7A and S7B), and some reduction in the paraventricular nuclei (Figures S7C and S7D), sparing other brain regions (e.g., the thalamus and hippocampus) (Figures S7C and S7D). Over the first 7 weeks of the treatment period, food intake remained stable in these aged mice (Figure S8A), while a slight trend of decreased body weight was observed only in the exenatide-treated scramble shRNA control group (Figure S8B). No significant differences in glucose tolerance were found among the groups after the 13-week treatment period (Figure S8C). Although not statistically significant, the changes in gonadal fat weight were consistent with the expected effects of *Glp1r* knockdown (i.e., higher percentage of body weight with hypothalamic *Glp1r* knockdown) and GLP-1RA treatment (i.e., lower with exenatide treatment) (Figure S8D).

Consistent with the previous findings, we observed widespread age-counteracting transcriptomic effects of exenatide treatment in the hippocampus, frontal cortex, circulating WBCs, heart, and skeletal muscle (Figures 5C and 5D). Interestingly, these effects appeared to be even stronger in this cohort of mice where treatment was delivered at an older age (i.e., from 18 to 21 months old). This was evidenced on differential expression (Figures 5C and 5D) and permutation sensitivity analysis (Figure S9A), particularly clear shifts of aged exenatide treatment group data points toward the young vehicle group on PCA despite some across-sample variance (Figure S8H), as well as differentially expressed gene modules revealed by WGCNA (Figures 5E, S4C, and S4D), in all tissue organs profiled (i.e., hippocampus, frontal cortex, circulating WBCs, heart, and skeletal muscle), compared with the earlier treatment cohort (cf. Figures 2B, 2E–2G, 3E, S2A, S3A, S3B, and S4A). Among exenatide-upregulated gene modules counteractive to aging (hippocampus modules 2, 8; frontal cortex module 10; circulating WBCs module 13; skeletal muscle modules 5, 7, and 15), we found significant enrichment of principally genes associated with protein translation/proteostasis and lysosome/autophagy/mitophagy (Figures 5E and S4D). For exenatide-downregulated modules opposing aging effect (hippocampus modules 1 and 9; circulating WBCs module 10; heart module 3; skeletal muscle module 4), apart from the functional pathways shared with upregulated modules, we also noted enrichment of genes involved in inflammatory response and senescence (Figures 5E and S4D).

The counteraction of age-related transcript expression changes induced by exenatide treatment in the hippocampus remained similarly strong after knocking down hypothalamic *Glp1r* (Figures 5F, 5G, and S8E). However, in the frontal cortex, circulating WBCs, heart, and skeletal muscle, the transcriptomic age-counteracting effects of exenatide treatment were weakened or even abolished by the *Glp1r* knockdown (Figures 5F, 5G, and S8E). This was evidenced qualitatively by an overall lack of negative correlations when comparing aging and exenatide treatment effects under hypothalamic *Glp1r* knockdown (Figure 5F), in contrast to the presence of permutation analysis-backed anti-correlations across these tissue organs and circulating WBCs (Figures 5C and S9A). Intriguingly, exenatide treatment even exacerbated some age-related transcript expression changes

(D) Functional pathway terms enrichment among aging-associated transcripts with differential expressions that were counteracted by exenatide treatment across the different tissue organs and circulating WBCs.

(E) Weighted gene co-expression network analysis (WGCNA) with heatmap showing the normalized eigengene expression levels of significant differentially expressed modules with aging and/or exenatide treatment across animals in the different experimental groups. Gray squares represent missing values as not all animals had all tissues successfully profiled.

(F and G) Dot plots showing the enrichment of gene sets associated with various hallmarks of aging, among the exenatide treatment-induced differentially expressed modules in the tissue organs and circulating WBCs. Significant exenatide-upregulated (F) and downregulated (G) modules with opposite significant changes in aging are annotated with green dots at the bottom.

Sample sizes in (A)–(D) for each tissue organ and circulating WBCs follow that specified in Figure 2. For WGCNA and module gene enrichment analyses in (E)–(G), n = 8, 9, and 8 mice (biological replicates) for the young adult vehicle, aged vehicle, and aged exenatide treatment groups, respectively.

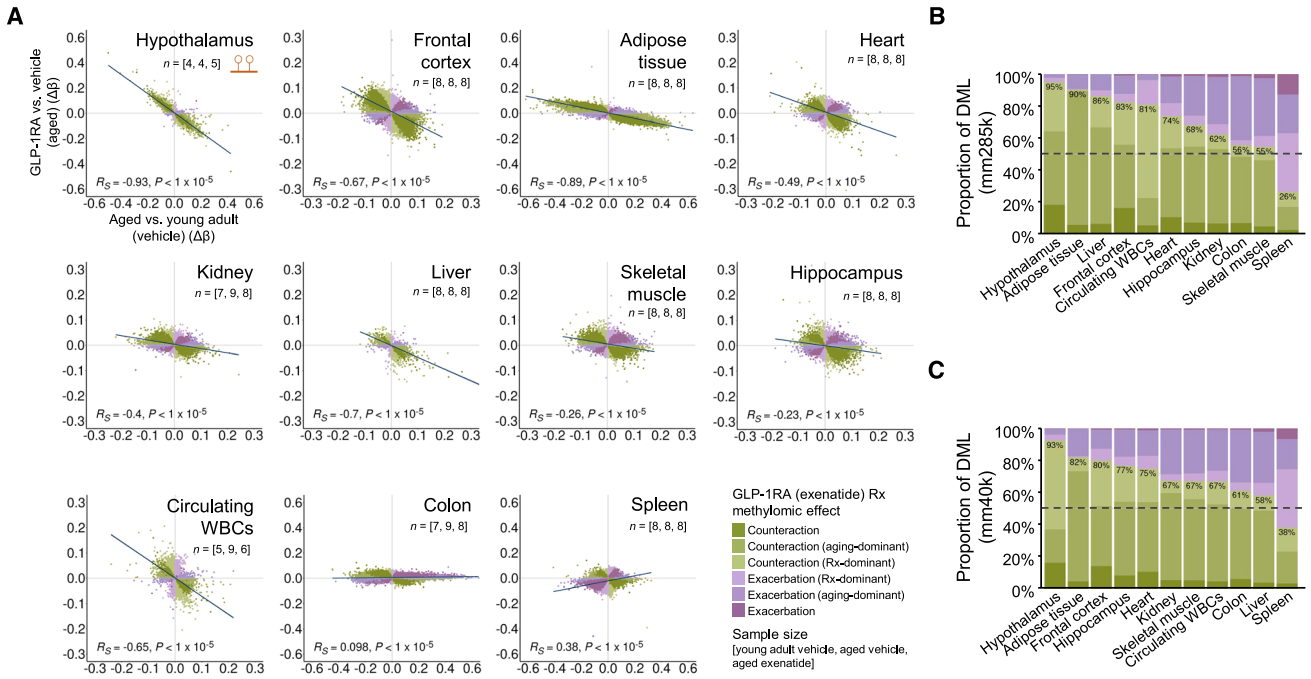

Figure 4. DNA methylomic changes in aging male mice treated with a GLP-1RA (exenatide) for 30 weeks starting at 11 months old

(A) Scatterplots showing DNA methylation (DNAm) level changes in aging (*x* axis) vs. exenatide treatment (*y* axis) at sites covered by the Illumina mouse 285k array (mm285k) across different tissue organs and circulating white blood cells (WBCs). Each dot represents one differentially methylated locus (DML), color-coded by treatment (Rx) effect categories as shown in the inset (counteraction, opposing aging and Rx effects; exacerbation, same aging and Rx effects; aging- or Rx-dominant, statistically significant in the respective comparison only; no additional label, significant for both aging and Rx effect comparisons; see also STAR Methods). For each plot, the line represents the linear fit. The Spearman correlation coefficients (R_S) and associated *p* values are also shown. Inset of left upper: symbol for DNAm. Sample sizes for the various tissue organs and circulating WBCs are specified in squared brackets (numbers of mice [biological replicates] for young adult vehicle, aged vehicle, and aged exenatide groups).

(B) Summary bar plot of the proportions of DML among the mm285k array sites under different categories (as specified in the inset of A).

(C) Similar to (B), but for DML among the imputed mammalian conserved sites covered by the mammalian 40k array (mm40k).

in the heart and skeletal muscle of the hypothalamic *Glp1r* knockdown mice (Figures 5F, 5G, and S8E).

We similarly found widespread counteraction of aging-associated DNAm changes by exenatide treatment in this cohort across the hippocampus, frontal cortex, circulating WBCs, heart, and skeletal muscles (Figure 5H). Additional sensitivity analysis indicated that this remained robust in the hippocampus, frontal cortex, circulating WBCs, and heart (Figure S9C), accompanied by generally consistent DNAm age clock changes associated with treatment, though statistical significance in age clocks reduction was observed only in the hippocampus (Figure S5C). The age-counteracting differential methylation changes was strongly attenuated in animals with hypothalamic *Glp1r* knockdown in the examined tissue organs and circulating WBCs (Figures 5I and S8F). This exhibited qualitatively as a lack of consistent negative correlations between aging and treatment effects on the methylomes (Figure 5I), unlike in hypothalamic *Glp1r*-intact mice where there was a uniform pattern of anti-correlations supported by permutation analysis (Figures 5H and S9C). Notably, this occurred even in the hippocampus (Figures 5I and S8F), despite the preservation of age-counteracting transcriptomic impact (Figures 5F and 5G). Although the modest age-counteracting effect of exenatide treatment on the circulating metabolome (Figure 5J) appeared to be generally consistent with or without hypothalamic *Glp1r* knockdown (Figure S8G), the negative correlation between aging- and exenatide treatment-associated effects was diminished in the mice with *Glp1r* knockdown (Figure 5K).

Based on these results, we concluded that hypothalamic GLP-1R is crucial in mediating the molecular age-counteracting effects of GLP-1RA treatment throughout the body. These data support the notion that the beneficial outcomes of GLP-1RA treatment are dependent on the activation of hypothalamic GLP-1R, which in turn contributes to the systemic counteraction of aging.

GLP-1R agonism and mTOR inhibition modulate multi-omic landscapes along shared and distinct axes in aging

As mTOR inhibition represents the strongest known anti-aging pharmacological intervention, we reasoned that establishing GLP-1R agonism as an anti-aging strategy would benefit from benchmarking against mTOR inhibition. Given the molecular age-counteracting effects of GLP-1RA and the known anti-aging effects of mTOR inhibition,[1,66] this comparison would allow us to determine their relative potencies and reveal potential phenotypic and/or mechanistic convergence. To this end, we included an additional experimental group of animals (*n* = 5 male mice) treated with rapamycin (8 mg/kg bw/2 days i.p., starting at 18 months old and continued for 13 weeks; Figure 5A), from which we obtained identical metabolic and molecular readouts

CellPress
OPEN ACCESS

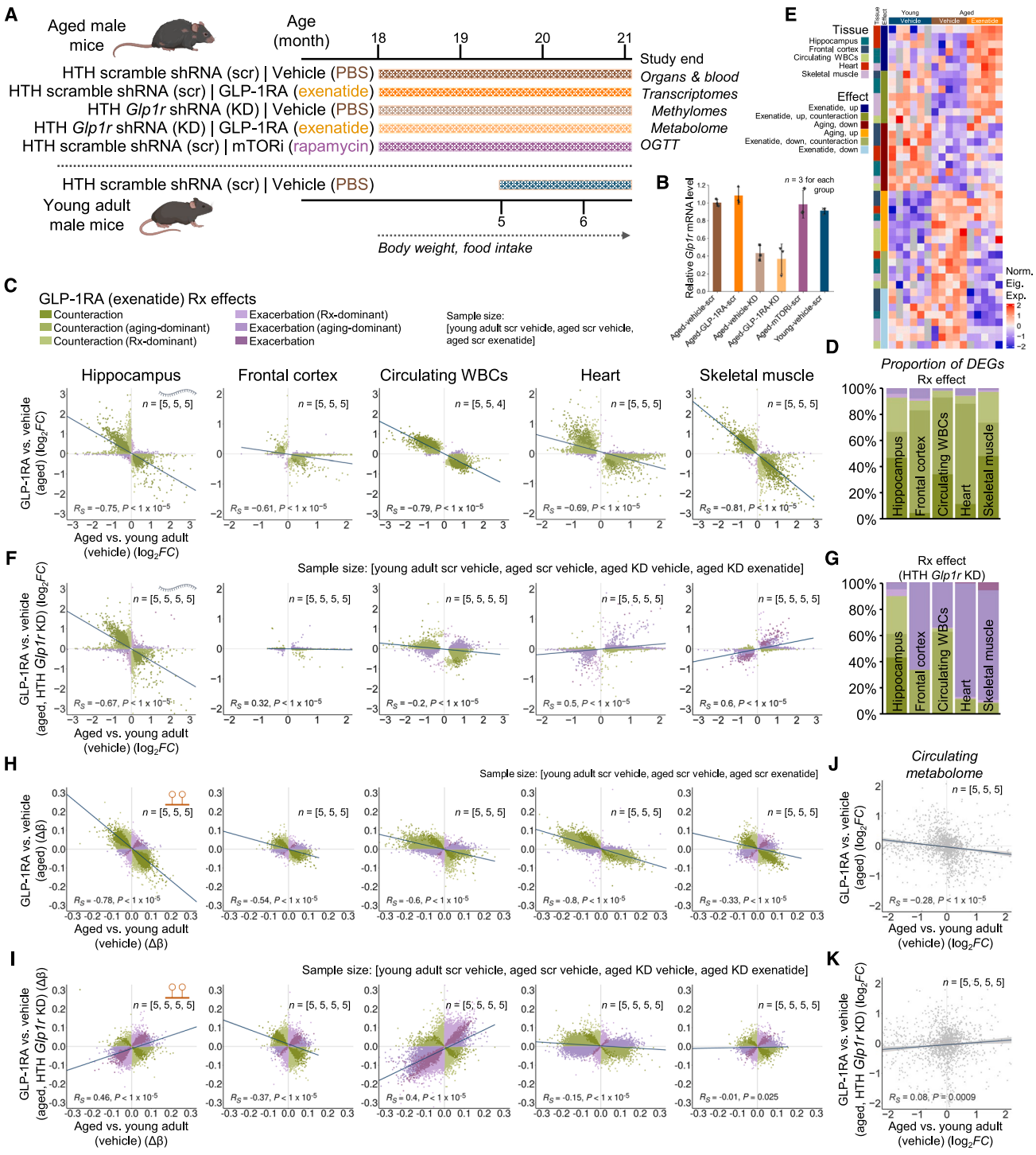

Figure 5. Age-counteracting transcriptomic, methylomic, and metabolomic effects of 13-week GLP-1RA (exenatide) treatment in aged male mice starting at 18 months old and the dependence on hypothalamic GLP-1R

(A) Schematic of experimental design for the aged short-term treatment cohort. The animals received bilateral hypothalamic injection of adeno-associated virus vector (AAV) either for the expression of shRNA to knockdown (KD) *Glp1r* or scramble shRNA (scr), and received phosphate-buffered saline (PBS) vehicle, exenatide, or rapamycin treatment. HTH, hypothalamus; OGTT, oral glucose tolerance test.

(B) Mean (±SD) hypothalamic *Glp1r* transcript expression levels measured with quantitative PCR ($n = 3$ mice [biological replicates] from each group used for this comparison), relative to the mean of the aged control group (i.e., hypothalamic scramble shRNA AAV injection, treated with vehicle).

(C) Scatterplots showing transcriptomic changes in aging (*x* axis) vs. exenatide treatment (*y* axis) in different tissue organs and circulating white blood cells (WBCs). Each dot represents one differentially expressed gene (DEG), color-coded by treatment (Rx) effect categories as shown in the inset (counteraction,

(legend continued on next page)

(Figures 5A, 5B, and S8A–S8D). Consistent with the known effects of mTOR inhibition,[66] rapamycin treatment led to a slight trend of decreased food intake (Figure S8A) and body weight (Figure S8B), significant impairment in glucose tolerance[67] (Figure S8C), and reduction in gonadal fat (Figure S8D).

The age-counteracting effects of rapamycin were evident in the transcriptomes (Figures 6A, 6B, S8H, and S9B) and DNA methylomes (Figures 6C and S9D) of the hippocampus, frontal cortex, circulating WBCs, heart, and skeletal muscle, as well as in the circulating metabolome (Figure 6D). These multi-tissue effects support and extend previous findings on rapamycin's strong counteraction of aging, including age-related changes in skeletal muscle transcriptome[68] and hippocampal DNA methylome.[69] Remarkably, the effects of exenatide treatment correlated well with those observed with rapamycin at transcriptomic, methylomic, and circulating metabolomic levels (Figures 6E–6G). Their efficacies appeared similarly potent, as reflected by the transcriptomic and methylomic changes in the hippocampus, circulating WBCs, heart, and skeletal muscle (Figures 5C, 5D, 5H, 6A–6C, 6E, 6F, and S8H). A high similarity of the transcriptomic effects of exenatide and rapamycin across all these tissues and circulating WBCs was also strongly supported by permutation sensitivity analysis (Figure S10A), whereas for DNA methylome the positive correlations were more robust for the hippocampus, circulating WBCs, and skeletal muscle (Figure S10B). In addition, rapamycin treatment had similar impacts on DNAm age clocks as exenatide treatment, including the reduction of a DNAm age clock in the hippocampus (Figure S5C). In the skeletal muscle, exenatide appeared to induce even strong molecular age-counteraction in the transcriptome (Figures 5C, 5D, 6A, 6B, S8H, S9A, and S9B). Meanwhile, rapamycin exhibited a stronger impact on the frontal cortex transcriptome (Figures 5C, 5D, 6A, and 6B) and the circulating metabolome (Figures 5J, 6D, and 6G).

Finally, we performed WGCNA on the transcriptomic data to explore the functional gene modules affected either commonly or distinctively by treatments with exenatide and rapamycin. The analysis corroborated the substantial transcriptomic concordance induced by the two treatments, with numerous shared differentially expressed gene modules (Figure 6H). While we also noted that unique gene modules were significantly altered by each treatment, the overall directionality of expression changes was consistent (Figure 6H). Pathway analysis revealed treatment- and tissue-specific effects, with exenatide preferentially upregulating genes involved in mitochondrial energy metabolism within the hippocampus (Figure 6I) and downregulating Notch signaling-related genes in skeletal muscle (Figure 6J). Conversely, rapamycin more strongly enhanced gene expressions influencing energy metabolism in the heart (Figure 6I). Hence, while exenatide and rapamycin phenocopy each other's effects, they also modulate age-related molecular changes in a tissue-specific and treatment-dependent manner.

DISCUSSION

Here, we show that GLP-1R agonism is a promising strategy for the mitigation of age-related decline and extension of healthspan. Encouragingly, the age-counteracting effects of GLP-1RA treatment are widespread, spanning across tissues of the whole body, the circulatory system, and multiple molecular layers as demonstrated by our multi-omic assays. It has been proposed that differentiating between rate, baseline, and combined models in anti-aging interventions allows us to identify whether they target aging mechanisms directly, mimic the targeting of aging processes, or have a mixed effect,[70,71] respectively. Based on our data, the largely specific functional and molecular responses to exenatide treatment in aged mice compared with their young adult counterparts align with a necessary, though not sufficient, condition for a rate model of anti-aging with GLP-1R agonism. Crucially, in our experiments, we selected the dosage of exenatide to minimize potential confounders, in particular aiming to achieve the age-counteracting effects without significantly influencing food intake or body weight. We acknowledge that a larger sample size might still reveal statistically significant differences in body weight change when comparing exenatide vs. vehicle groups. Note however that the subtle absolute difference we observed suggest that the functional and molecular impacts could be largely attributed to the weight loss-independent pharmacological effects of GLP-1R agonism. In addition, we did not observe significant cognitive benefits in our relatively small aging long-term treatment cohort and did not assess long-term memory retention or cognitive changes in even older mice. Therefore, while the full spectrum of benefits from GLP-1RA in aging may be more

opposing aging and Rx effects; exacerbation, same aging and Rx effects; aging- or Rx-dominant, statistically significant in the respective comparison only; no additional label, significant for both aging and Rx effect comparisons; see also STAR Methods). Inset of left: symbol for transcript.

(D) Summary bar plot of the proportions of DEGs under different categories (as specified in the inset of C).

(E) Weighted gene co-expression network analysis (WGCNA) with heatmap showing the normalized eigengene expression levels (Norm. Eig. Exp.) of significant differentially expressed modules with aging and/or exenatide treatment across animals in the different experimental groups. n = 6, 5, and 5 biological replicates for the young adult vehicle, aged vehicle, and aged exenatide treatment groups, respectively, for this analysis. Gray squares represent missing values as not all animals had all tissues successfully profiled.

(F and G) Similar to (C) and (D), but showing exenatide treatment effects in aged animals with hypothalamic *Glp1r* KD.

(H) Scatterplots showing DNA methylation (DNAm) level changes in aging (x axis) vs. exenatide treatment (y axis) at sites covered by the Illumina mouse 285k array (mm285k) across different tissue organs and circulating WBCs. Each dot represents one differentially methylated locus (DML), color-coded by treatment (Rx) effect categories (as shown in the inset of C). Inset of left: symbol for DNAm.

(I) Similar to (H), but showing exenatide treatment effects in aged animals with hypothalamic *Glp1r* KD.

(J) Scatterplot showing plasma metabolomic changes in aging (x axis) vs. exenatide treatment (y axis). Each dot represents one metabolite.

(K) Similar to (J), but showing exenatide treatment effects in aged animals with hypothalamic *Glp1r* KD.

In (C), (F), and (H)–(K), the lines represent linear fits (with confidence interval [gray] in J and K). The Spearman correlation coefficients (R_S) and associated p values are also shown. Sample sizes (specified in squared brackets) for data in (C), (D), and (F)–(K): n = 5 biological replicates for each experimental group for each profiling, except n = 4 aged exenatide-treated biological replicates (scr group) for circulating WBCs transcriptomic profiling.

CellPress
OPEN ACCESS

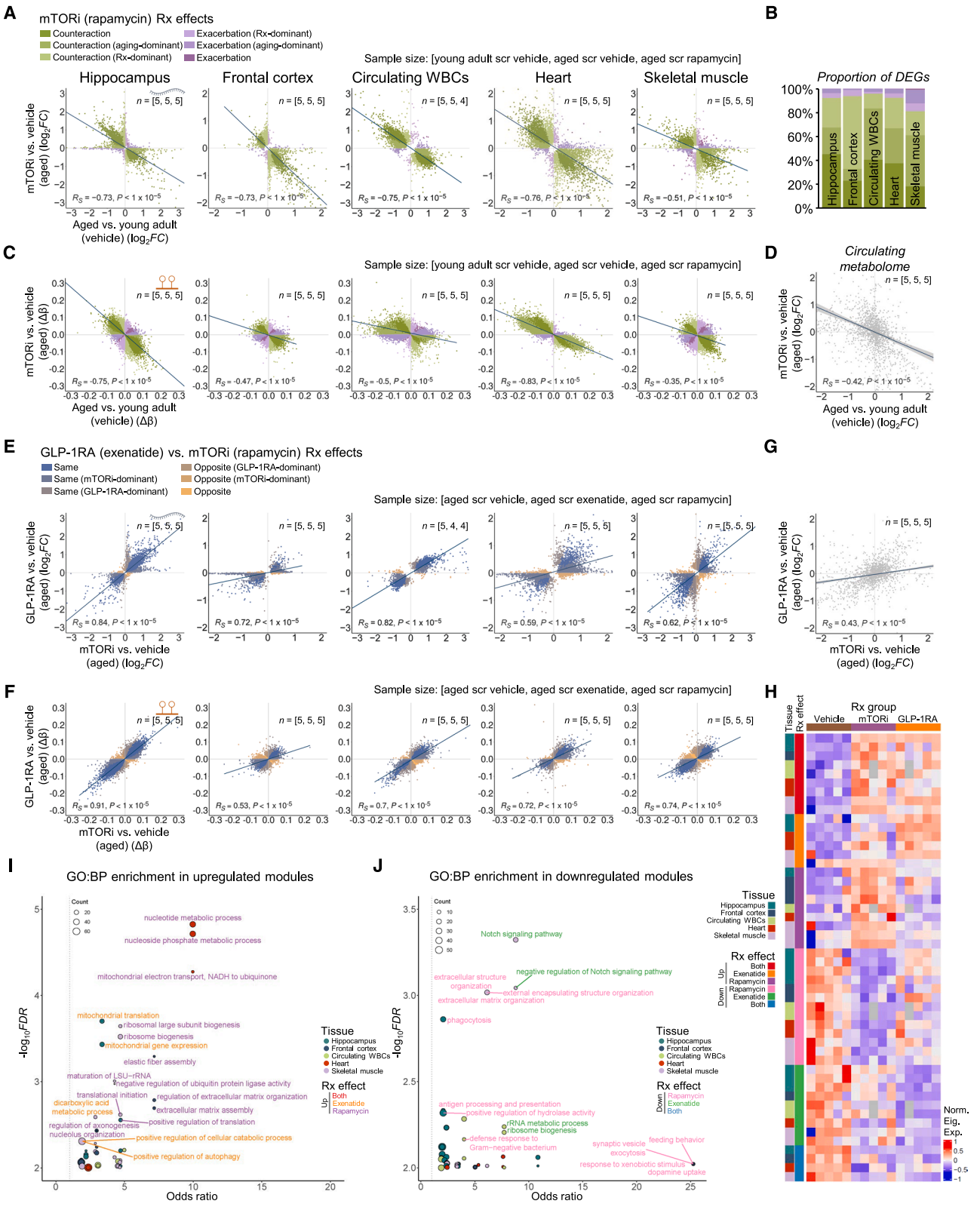

(legend on next page)

substantial at higher dosages, it remains to be elucidated whether the observed molecular impacts translate into cognitive improvements.

The mechanisms underlying the observed effects are undoubtedly complex, given that systemically administered exenatide activates GLP-1R at various body sites. For example, GLP-1RA enhances the firing of GLP-1R-expressing pro-opiomelanocortin ($POMC^{GLP\text{-}1R+}$) neurons in the arcuate nucleus of the hypothalamus.[72,73] The significant reliance of the observed age-counteracting molecular effects on hypothalamic GLP-1R suggests that GLP-1RA-driven age-counteraction may depend on modulating hypothalamic $POMC^{GLP\text{-}1R+}$ neuronal activities. In addition, potential systemic impacts mediated by glial GLP-1R activation need to be considered.[74,75] Our findings are in line with previous studies indicating that CNS GLP-1R is an essential component of the signaling network mediating not only neurological[76–78] but also systemic anti-inflammatory actions of GLP-1RA.[79] The brain, similar to other body organs, is inevitably impacted by peripheral organs and circulatory changes in aging.[80–83] Conversely, brain aging affects its coordinating role in body-wide processes.[84,85] These all underscore the profound influence of the CNS on systemic health and suggest that optimizing CNS exposure could be advantageous for the design of new drugs targeting or co-targeting GLP-1R.

Interestingly, in the animals treated from middle age (i.e., 11 months old for 30 weeks), we found a divergence in omic impacts in some organs, with the colon DNA methylome being less responsive to GLP-1RA treatment compared with substantial transcriptional changes, and the opposite pattern in the liver and kidneys. Moreover, after hypothalamic *Glp1r* knockdown in even older animals, strong age-counteracting effects in the hippocampus persisted in the transcriptome, but not in the DNAm profile. A divergence of molecular responses is also reflected in the DNAm age clock analysis. While the multi-tissue, multi-omic profiling revealed consistent age-counteracting patterns based on differential expression comparisons with permutation sensitivity tests, PCA and WGCNA, these did not translate to a strong reduction of DNAm age clocks. Nevertheless, exenatide treatment did significantly decrease two established DNAm age clocks in the hippocampus of the older, short-term treatment cohort. The DNAm age clocks, which rely on a specific subset of CpG sites, therefore did not fully capture the broader age-counteracting effects observed across the methylome and transcriptome. In addition, these findings imply that the effects of GLP-1R agonism on transcript expression may involve other epigenetic or gene expression regulatory mechanisms that are body-site specific. As we observed generally stronger molecular age-counteracting transcriptomic and methylomic effects in the brain, heart, skeletal muscle, and circulating WBCs in the older animals, it raises the question of whether the omic responses with GLP-1R agonism might become more convergent at an even more advanced age.

We found substantial similarity of multi-omic impacts between exenatide and rapamycin. This raises the need to systematically explore the relative advantages and disadvantages of adopting GLP-1R agonism vs. mTOR inhibition. At the preclinical level, it would be necessary to investigate how each approach might yield different anti-aging efficacies across various organ systems and cell types. Additionally, examining potential overlaps in their mechanisms of action, such as effects on POMC neurons and other modulatory effects in the CNS,[86,87] would be valuable. Past and ongoing clinical studies are actively evaluating the anti-aging potential of mTOR inhibition.[88,89] It remains to be seen whether there are overlapping clinical benefits, taking into account the side effect profiles of each drug class. While concerns about skeletal muscle loss have been raised for higher doses of GLP-1RAs used in obesity treatment, our study was designed with a largely weight-neutral dose to isolate weight loss-independent effects and mechanisms. Our findings therefore highlight the potential for achieving age-counteracting benefits in muscle within a relatively low-dose context. Whether these benefits may generalize to and persist at higher, clinically used

Figure 6. Age-counteracting molecular effects of 13-week GLP-1RA (exenatide) treatment vs. that of mTOR inhibition (rapamycin) in aged male mice starting at 18 months old

(A) Scatterplots showing transcriptomic changes in aging (*x* axis) vs. rapamycin treatment (*y* axis) in different tissue organs and circulating white blood cells (WBCs). Each dot represents one differentially expressed gene (DEG), color-coded by treatment (Rx) effect categories as shown in the inset (counteraction, opposing aging and Rx effects; exacerbation, same aging and Rx effects; aging- or Rx-dominant, statistically significant in the respective comparison only; no additional label, significant for both aging and Rx effect comparisons; see also STAR Methods). Inset of left: symbol for transcript.

(B) Summary bar plot of the proportions of DEGs under different categories (as specified in the inset of A).

(C) Scatterplots showing DNA methylation (DNAm) level changes in aging (*x* axis) vs. exenatide treatment (*y* axis) at sites covered by the Illumina mouse 285k array (mm285k) across different tissue organs and circulating WBCs. Each dot represents one differentially methylated locus (DML), color-coded by treatment Rx effect categories (as shown in the inset of A). Inset of left: symbol for DNAm.

(D) Scatterplot showing plasma metabolomic changes in aging (*x* axis) vs. rapamycin treatment (*y* axis). Each dot represents one metabolite.

(E–G) Scatterplots showing transcriptomic (E), DNAm level (F), and plasma metabolomic (G) changes with rapamycin (*x* axis) vs. exenatide (*y* axis) treatment. Inset of (E): DEG and DML categories, indicating same or opposite Rx effects; GLP-1RA- or mTORi-dominant, statistically significant in the respective comparison only; no additional label, significant for both Rx effect comparisons (see also STAR Methods). Inset of left of (E) and (F): symbols for transcript and DNAm, respectively. In (A) and (C)–(G), the lines represent linear fits (with confidence interval [gray] in D and G). The Spearman correlation coefficients (R_S) and associated *p* values are also shown.

(H) Heatmap showing the normalized eigengene expression (Norm. Eig. Exp.) levels of significant differentially expressed modules with exenatide and/or rapamycin treatment. Inset (left) shows the color coding for tissue origin and Rx effect category (i.e., significant with exenatide, rapamycin, or both treatments). Gray squares represent missing values as not all animals had all tissues successfully profiled.

(I) Bubble chart showing the Gene Ontology-Biological Process (GO:BP) pathways with significant enrichment among the different treatment-upregulated gene modules with exenatide and/or rapamycin treatment (top 3 for each tissue organ/circulating WBCs plotted). Gene count is represented with bubble size. Tissue origin and Rx effect category are color-coded as per the inset.

(J) Similar to (I), but for treatment-downregulated gene modules. Sample sizes (specified in squared brackets) for all plots: $n = 5$ mice (biological replicates) for each experimental group for each profiling, except $n = 4$ aged exenatide- and 4 rapamycin-treated (scr groups) biological replicates for circulating WBC transcriptomic profiling.

doses remains an important and distinct question for further investigations.

Given the extensive range of age-counteracting effects observed, it will be important to evaluate the potential of GLP-1RAs in treating human age-related diseases beyond the current clinical indications for diabetes, obesity, and their associated comorbidities. Ongoing phase 3 trials are investigating the use of GLP-1RA in treating Alzheimer's disease,[90] while we are also conducting a pilot trial focused on cerebral small vessel disease (ClinicalTrials.gov identifier: NCT05356104). Our findings also open the avenue for a therapeutic strategy that combines a GLP-1RA or mTOR inhibitor with molecular entities that engage disease-specific molecular targets or address issues of selective vulnerability.[91] For instance, combining a GLP-1RA with an anti-amyloid agent[92,93] for Alzheimer's disease treatment could be advantageous, where the GLP-1RA may also serve as a pretreatment or as an adjunct therapy once brain amyloid levels are normalized. However, mechanistic compatibility will need to be experimentally verified for each specific combination of therapeutic approaches and in individual clinical conditions. This approach may allow us to leverage synergistic anti-aging and neuroprotective effects to combat complex, multifactorial age-related conditions.

Collectively, our work has provided multifaceted evidence for a comprehensive body-wide anti-aging strategy based on GLP-1R agonism, which, given its current clinical use and favorable safety profile, introduces a readily testable anti-aging intervention for a range of age-related conditions. Future longitudinal studies are necessary to explore whether GLP-1R agonism may complement other anti-aging methods.

Limitations of the study

We acknowledge that our study has several limitations. First, we have not demonstrated lifespan extension in mice. While the strong similarities with the effects of mTOR inhibition, which is well proven for its longevity benefits,[1,66] suggest that GLP-1R agonism may prolong lifespan, this hypothesis remains to be tested experimentally. Second, although the clinically reported cardiorenal[94–96] and pleiotropic[33–35,37] benefits of GLP-1RAs have been similar across sexes, we performed experiments only in male mice. Given that anti-aging interventions can exhibit sex-dependent effects, additional experiments are needed to rigorously test generalizability across sexes. Third, the detailed cellular mechanisms behind the age-counteraction observed with GLP-1RA treatment and their downstream effects on age-related biological pathways remain unclear. Future research employing single-cell and spatial omics profiling, along with appropriate functional and histological assays, is required to address these gaps. Resolving these limitations will help identify cell-type-specific age-counteracting effects, clarify the full impact of GLP-1R agonism on aging, and inform the design of clinical trials.

RESOURCE AVAILABILITY

Lead contact

Further information and requests for resources and reagents should be directed to the lead contact, Ho Ko (ho.ko@cuhk.edu.hk).

Materials availability

The custom-generated plasmids and AAVs in this study will be made available on request, but we may require a payment and/or a completed materials transfer agreement if there is potential for commercial application. All other materials used in this study that are commercially available are specified in the key resources table.

Data and code availability

The raw and pre-processed data have been deposited and are available at SRA: PRJNA1177532 and GEO: GSE280382 (RNA sequencing data) and GEO: GSE279437 (DNAm data). Numerical values that were used to create all plots in the paper are available in Data S1. Custom-written codes for data analysis are available on Zenodo (https://zenodo.org/records/15696759).

ACKNOWLEDGMENTS

We thank Tom Mrsic-Flogel and Tom Otis for helpful discussions about the study. We thank Phil Xie for advice on DNAm analysis and helpful comments on the manuscript. We thank Anki Miu, Dorothy Ieong, Becky Yung, and Florence Yau for administrative support to the project. We acknowledge access to TissueLyser II at Jun Yu's lab, behavioral box at Hei Ming Lai's lab, and support for use of QuantStudio 12K Flex by the core facility management team of the Li Ka Shing Institute of Health Sciences. This work was supported by the Lo's Family Charity Fund Limited, Margaret K. L. Cheung Research Centre for Management of Parkinsonism center fund, the Asian Young Scientist Fellowship, a Croucher Innovation Award (CIA20CU01) from the Croucher Foundation, a Hong Kong PhD Fellowship, the General Research Fund (14100122), the Collaborative Research Fund (C6027-19GF, C7074-21GF, and C4062-22EF), the Area of Excellence Scheme (AoE/M-604/16) of the Research Grants Council of the University Grants Committee of Hong Kong, the Excellent Young Scientists Fund (Hong Kong and Macau) (82122001), and the Young Scientists Fund (82201503) from the National Natural Science Foundation of China. The graphical abstract was designed by Jennifer Ma.

AUTHOR CONTRIBUTIONS

Conceptualization, J.H., A.J.K., V.C.T.M., and H.K.; methodology, J.H., A.J.K., V.C.T.M., and H.K.; investigation, J.H., A.J.K., J.C.Y.L., C.L.H.C., B.Y.I., L.Y.T., R.C.H.C., D.C.W.C., Z.W., X.Z., H.T.C., M.P.S.L., Z.L., N.L., M.W., L.Y.C.Y., W.K.K.W., K.H.-M.C., W.-J.L., Y.T., Y.Z., W.S., B.W.-L.N., S.H.W., T.W.L., and H.K.; data curation, J.H., A.J.K., J.C.Y.L., C.L.H.C., R.C.H.C., and D.C.W.C.; formal analysis, J.H., A.J.K., J.C.Y.L., C.L.H.C., L.Y.T., R.C.H.C., D.C.W.C., and H.K.; software, J.H., A.J.K., J.C.Y.L., L.Y.T., R.C.H.C., D.C.W.C., Z.W., M.W., and H.K.; validation, J.H., A.J.K., and H.K.; visualization, J.H., A.J.K., J.C.Y.L., and H.K.; funding acquisition, J.H., V.C.T.M., and H.K.; resources, J.H., A.J.K., D.C.W.C., V.C.T.M., and H.K.; supervision, J.H., A.J.K., V.C.T.M., and H.K.; writing – original draft, J.H., A.J.K., V.C.T.M., and H.K.; writing – review and editing, all authors; project administration, J.H., A.J.K., V.C.T.M., and H.K.; all authors approved the article.

DECLARATION OF INTERESTS

Chinese University of Hong Kong (CUHK) filed a patent application in part based on results reported in this study, with J.H., A.J.K., J.C.Y.L., C.L.H.C., and H.K. listed as inventors. J.H., V.C.T.M., and H.K. are founders and own equity in Memora Sciences Limited.

STAR★METHODS

Detailed methods are provided in the online version of this paper and include the following:

- KEY RESOURCES TABLE
- EXPERIMENTAL MODEL AND SUBJECT DETAILS
  - Experimental Animals
- METHOD DETAILS
  - Exendin-4 and rapamycin treatment
  - AAV-mediated hypothalamic Glp1r knockdown

- Immunohistochemistry for validation of *Glp1r*/GLP-1R knockdown
- Forelimb grip strength test
- Accelerated rotarod test
- Barnes maze
- Open-field test and frailty index
- Y-maze
- Statistical tests for physical and cognitive tests
- Metabolic assessment
- Statistical software for assessing physical, behavioral, and metabolic readouts
- Tissue collection and storage
- Total RNA and genomic DNA extraction
- RNA sequencing
- Plasma metabolomic measurement
- Bioinformatic data analysis
- Metabolome data analysis
- RNA-sequencing data analysis
- Principal component analysis (PCA)
- Weighted gene co-expression network analysis
- Pathway enrichment analysis
- DNA methylation analysis
- Epigenetic age clock analysis
- Permutation sensitivity analysis

SUPPLEMENTAL INFORMATION

Supplemental information can be found online at https://doi.org/10.1016/j.cmet.2025.10.014.

Received: October 30, 2024
Revised: June 17, 2025
Accepted: October 28, 2025
Published: November 19, 2025

REFERENCES

1. Mannick, J.B., and Lamming, D.W. (2023). Targeting the biology of aging with mTOR inhibitors. Nat. Aging *3*, 642–660. https://doi.org/10.1038/s43587-023-00416-y.
2. Kaeberlein, M., and Galvan, V. (2019). Rapamycin and Alzheimer's disease: Time for a clinical trial? Sci. Transl. Med. *11*, eaar4289. https://doi.org/10.1126/scitranslmed.aar4289.
3. Chaib, S., Tchkonia, T., and Kirkland, J.L. (2022). Cellular senescence and senolytics: the path to the clinic. Nat. Med. *28*, 1556–1568. https://doi.org/10.1038/s41591-022-01923-y.
4. Gasek, N.S., Kuchel, G.A., Kirkland, J.L., and Xu, M. (2021). Strategies for targeting senescent cells in human disease. Nat. Aging *1*, 870–879. https://doi.org/10.1038/s43587-021-00121-8.
5. Rajman, L., Chwalek, K., and Sinclair, D.A. (2018). Therapeutic potential of NAD-boosting molecules: the in vivo evidence. Cell Metab. *27*, 529–547. https://doi.org/10.1016/j.cmet.2018.02.011.
6. Verdin, E. (2015). NAD^+ in aging, metabolism, and neurodegeneration. Science *350*, 1208–1213. https://doi.org/10.1126/science.aac4854.
7. Damgaard, M.V., and Treebak, J.T. (2023). What is really known about the effects of nicotinamide riboside supplementation in humans. Sci. Adv. *9*, eadi4862. https://doi.org/10.1126/sciadv.adi4862.
8. Singh, P., Gollapalli, K., Mangiola, S., Schranner, D., Yusuf, M.A., Chamoli, M., Shi, S.L., Lopes Bastos, B.L., Nair, T., Riermeier, A., et al. (2023). Taurine deficiency as a driver of aging. Science *380*, eabn9257. https://doi.org/10.1126/science.abn9257.
9. Bordone, L., and Guarente, L. (2005). Calorie restriction, SIRT1 and metabolism: understanding longevity. Nat. Rev. Mol. Cell Biol. *6*, 298–305. https://doi.org/10.1038/nrm1616.
10. Spadaro, O., Youm, Y., Shchukina, I., Ryu, S., Sidorov, S., Ravussin, A., Nguyen, K., Aladyeva, E., Predeus, A.N., Smith, S.R., et al. (2022). Caloric restriction in humans reveals immunometabolic regulators of health span. Science *375*, 671–677. https://doi.org/10.1126/science.abg7292.
11. Ma, S., Sun, S., Geng, L., Song, M., Wang, W., Ye, Y., Ji, Q., Zou, Z., Wang, S., He, X., et al. (2020). Caloric restriction reprograms the single-cell transcriptional landscape of Rattus norvegicus aging. Cell *180*, 984–1001.e22. https://doi.org/10.1016/j.cell.2020.02.008.
12. Yücel, A.D., and Gladyshev, V.N. (2024). The long and winding road of reprogramming-induced rejuvenation. Nat. Commun. *15*, 1941. https://doi.org/10.1038/s41467-024-46020-5.
13. Lu, Y., Brommer, B., Tian, X., Krishnan, A., Meer, M., Wang, C., Vera, D.L., Zeng, Q., Yu, D., Bonkowski, M.S., et al. (2020). Reprogramming to recover youthful epigenetic information and restore vision. Nature *588*, 124–129. https://doi.org/10.1038/s41586-020-2975-4.
14. Villeda, S.A., Plambeck, K.E., Middeldorp, J., Castellano, J.M., Mosher, K.I., Luo, J., Smith, L.K., Bieri, G., Lin, K., Berdnik, D., et al. (2014). Young blood reverses age-related impairments in cognitive function and synaptic plasticity in mice. Nat. Med. *20*, 659–663. https://doi.org/10.1038/nm.3569.
15. Katsimpardi, L., Litterman, N.K., Schein, P.A., Miller, C.M., Loffredo, F.S., Wojtkiewicz, G.R., Chen, J.W., Lee, R.T., Wagers, A.J., and Rubin, L.L. (2014). Vascular and neurogenic rejuvenation of the aging mouse brain by young systemic factors. Science *344*, 630–634. https://doi.org/10.1126/science.1251141.
16. Chen, X., Luo, Y., Zhu, Q., Zhang, J., Huang, H., Kan, Y., Li, D., Xu, M., Liu, S., Li, J., et al. (2024). Small extracellular vesicles from young plasma reverse age-related functional declines by improving mitochondrial energy metabolism. Nat. Aging *4*, 814–838. https://doi.org/10.1038/s43587-024-00612-4.
17. Leiter, O., Brici, D., Fletcher, S.J., Yong, X.L.H., Widagdo, J., Matigian, N., Schroer, A.B., Bieri, G., Blackmore, D.G., Bartlett, P.F., et al. (2023). Platelet-derived exerkine CXCL4/platelet factor 4 rejuvenates hippocampal neurogenesis and restores cognitive function in aged mice. Nat. Commun. *14*, 4375. https://doi.org/10.1038/s41467-023-39873-9.
18. Schroer, A.B., Ventura, P.B., Sucharov, J., Misra, R., Chui, M.K.K., Bieri, G., Horowitz, A.M., Smith, L.K., Encabo, K., Tenggara, I., et al. (2023). Platelet factors attenuate inflammation and rescue cognition in ageing. Nature *620*, 1071–1079. https://doi.org/10.1038/s41586-023-06436-3.
19. Park, C., Hahn, O., Gupta, S., Moreno, A.J., Marino, F., Kedir, B., Wang, D., Villeda, S.A., Wyss-Coray, T., and Dubal, D.B. (2023). Platelet factors are induced by longevity factor klotho and enhance cognition in young and aging mice. Nat. Aging *3*, 1067–1078. https://doi.org/10.1038/s43587-023-00468-0.
20. Pálovics, R., Keller, A., Schaum, N., Tan, W., Fehlmann, T., Borja, M., Kern, F., Bonanno, L., Calcuttawala, K., Webber, J., et al. (2022). Molecular hallmarks of heterochronic parabiosis at single-cell resolution. Nature *603*, 309–314. https://doi.org/10.1038/s41586-022-04461-2.
21. Kanbay, M., Copur, S., Ozbek, L., Mutlu, A., Cejka, D., Ciceri, P., Cozzolino, M., and Haarhaus, M.L. (2024). Klotho: a potential therapeutic target in aging and neurodegeneration beyond chronic kidney disease—a comprehensive review from the ERA CKD-MBD working group. Clin. Kidney J. *17*, sfad276. https://doi.org/10.1093/ckj/sfad276.
22. Ximerakis, M., Holton, K.M., Giadone, R.M., Ozek, C., Saxena, M., Santiago, S., Adiconis, X., Dionne, D., Nguyen, L., Shah, K.M., et al. (2023). Heterochronic parabiosis reprograms the mouse brain transcriptome by shifting aging signatures in multiple cell types. Nat. Aging *3*, 327–345. https://doi.org/10.1038/s43587-023-00373-6.
23. Mahmoudi, S., Xu, L., and Brunet, A. (2019). Turning back time with emerging rejuvenation strategies. Nat. Cell Biol. *21*, 32–43. https://doi.org/10.1038/s41556-018-0206-0.
24. Guarente, L., Sinclair, D.A., and Kroemer, G. (2024). Human trials exploring anti-aging medicines. Cell Metab. *36*, 354–376. https://doi.org/10.1016/j.cmet.2023.12.007.
25. Holst, J.J. (2007). The physiology of glucagon-like peptide 1. Physiol. Rev. *87*, 1409–1439. https://doi.org/10.1152/physrev.00034.2006.

26. Holt, M.K., and Rinaman, L. (2022). The role of nucleus of the solitary tract glucagon-like peptide-1 and prolactin-releasing peptide neurons in stress: anatomy, physiology and cellular interactions. Br. J. Pharmacol. *179*, 642–658. https://doi.org/10.1111/bph.15576.

27. Drucker, D.J. (2018). Mechanisms of action and therapeutic application of glucagon-like peptide-1. Cell Metab. *27*, 740–756. https://doi.org/10.1016/j.cmet.2018.03.001.

28. Yao, H., Zhang, A., Li, D., Wu, Y., Wang, C.-Z., Wan, J.-Y., and Yuan, C.-S. (2024). Comparative effectiveness of GLP-1 receptor agonists on glycaemic control, body weight, and lipid profile for type 2 diabetes: systematic review and network meta-analysis. BMJ *384*, e076410. https://doi.org/10.1136/bmj-2023-076410.

29. Ussher, J.R., and Drucker, D.J. (2023). Glucagon-like peptide 1 receptor agonists: cardiovascular benefits and mechanisms of action. Nat. Rev. Cardiol. *20*, 463–474. https://doi.org/10.1038/s41569-023-00849-3.

30. Sattar, N., Lee, M.M.Y., Kristensen, S.L., Branch, K.R.H., Prato, S.D., Khurmi, N.S., Lam, C.S.P., Lopes, R.D., McMurray, J.J.V., Pratley, R.E., et al. (2021). Cardiovascular, mortality, and kidney outcomes with GLP-1 receptor agonists in patients with type 2 diabetes: a systematic review and meta-analysis of randomised trials. Lancet Diabetes Endocrinol. *9*, 653–662. https://doi.org/10.1016/S2213-8587(21)00203-5.

31. Heerspink, H.J.L., Apperloo, E., Davies, M., Dicker, D., Kandler, K., Rosenstock, J., Sørrig, R., Lawson, J., Zeuthen, N., and Cherney, D. (2023). Effects of semaglutide on albuminuria and kidney function in people with overweight or obesity with or without type 2 diabetes: exploratory analysis from the STEP 1, 2, and 3 trials. Diabetes Care *46*, 801–810. https://doi.org/10.2337/dc22-1889.

32. Mosenzon, O., Schechter, M., and Leibowitz, G. (2021). Kidney outcomes with glucagon-like peptide-1 receptor agonists in patients with type 2 diabetes. Adv. Chronic Kidney Dis. *28*, 347–360. https://doi.org/10.1053/j.ackd.2021.04.005.

33. Cukierman-Yaffe, T., Gerstein, H.C., Colhoun, H.M., Diaz, R., García-Pérez, L.-E., Lakshmanan, M., Bethel, A., Xavier, D., Probstfield, J., Riddle, M.C., et al. (2020). Effect of dulaglutide on cognitive impairment in type 2 diabetes: an exploratory analysis of the REWIND trial. Lancet Neurol. *19*, 582–590. https://doi.org/10.1016/S1474-4422(20)30173-3.

34. Nørgaard, C.H., Friedrich, S., Hansen, C.T., Gerds, T., Ballard, C., Møller, D.V., Knudsen, L.B., Kvist, K., Zinman, B., Holm, E., et al. (2022). Treatment with glucagon-like peptide-1 receptor agonists and incidence of dementia: Data from pooled double-blind randomized controlled trials and nationwide disease and prescription registers. Alzheimers. Dement. *8*, e12268. https://doi.org/10.1002/trc2.12268.

35. Brauer, R., Wei, L., Ma, T., Athauda, D., Girges, C., Vijiaratnam, N., Auld, G., Whittlesea, C., Wong, I., and Foltynie, T. (2020). Diabetes medications and risk of Parkinson's disease: a cohort study of patients with diabetes. Brain *143*, 3067–3076. https://doi.org/10.1093/brain/awaa262.

36. Skriver, C., Friis, S., Knudsen, L.B., Catarig, A.-M., Clark, A.J., Dehlendorff, C., and Mørch, L.S. (2023). Potential preventive properties of GLP-1 receptor agonists against prostate cancer: a nationwide cohort study. Diabetologia *66*, 2007–2016. https://doi.org/10.1007/s00125-023-05972-x.

37. Wang, L., Wang, W., Kaelber, D.C., Xu, R., and Berger, N.A. (2024). GLP-1 receptor agonists and colorectal cancer risk in drug-naive patients with type 2 diabetes, with and without overweight/obesity. JAMA Oncol. *10*, 256–258. https://doi.org/10.1001/jamaoncol.2023.5573.

38. Wang, L., Berger, N.A., Kaelber, D.C., and Xu, R. (2024). Association of GLP-1 receptor agonists and hepatocellular carcinoma incidence and hepatic decompensation in patients with type 2 diabetes. Gastroenterology *167*, 689–703. https://doi.org/10.1053/j.gastro.2024.04.029.

39. Lincoff, A.M., Brown-Frandsen, K., Colhoun, H.M., Deanfield, J., Emerson, S.S., Esbjerg, S., Hardt-Lindberg, S., Hovingh, G.K., Kahn, S.E., Kushner, R.F., et al. (2023). Semaglutide and cardiovascular outcomes in obesity without diabetes. N. Engl. J. Med. *389*, 2221–2232. https://doi.org/10.1056/NEJMoa2307563.

40. Athauda, D., and Foltynie, T. (2018). Protective effects of the GLP-1 mimetic exendin-4 in Parkinson's disease. Neuropharmacology *136*, 260–270. https://doi.org/10.1016/j.neuropharm.2017.09.023.

41. Du, H., Meng, X., Yao, Y., and Xu, J. (2022). The mechanism and efficacy of GLP-1 receptor agonists in the treatment of Alzheimer's disease. Front. Endocrinol. *13*, 1033479. https://doi.org/10.3389/fendo.2022.1033479.

42. Edison, P., Femminella, G.D., Ritchie, C.W., Holmes, C., Walker, Z., Ridha, B.H., Raza, S., Livingston, N.R., Nowell, J., Busza, G., et al. (2021). Evaluation of liraglutide in the treatment of Alzheimer's disease. Alzheimers Dement. *17*. https://doi.org/10.1002/alz.057848.

43. Gejl, M., Gjedde, A., Egefjord, L., Møller, A., Hansen, S.B., Vang, K., Rodell, A., Brændgaard, H., Gottrup, H., Schacht, A., et al. (2016). In Alzheimer's disease, 6-month treatment with GLP-1 analog prevents decline of brain glucose metabolism: randomized, placebo-controlled, double-blind clinical trial. Front. Aging Neurosci. *8*, 108. https://doi.org/10.3389/fnagi.2016.00108.

44. Athauda, D., Maclagan, K., Skene, S.S., Bajwa-Joseph, M., Letchford, D., Chowdhury, K., Hibbert, S., Budnik, N., Zampedri, L., Dickson, J., et al. (2017). Exenatide once weekly versus placebo in Parkinson's disease: a randomised, double-blind, placebo-controlled trial. Lancet *390*, 1664–1675. https://doi.org/10.1016/S0140-6736(17)31585-4.

45. Meissner, W.G., Remy, P., Giordana, C., Maltête, D., Derkinderen, P., Houéto, J.-L., Anheim, M., Benatru, I., Boraud, T., Brefel-Courbon, C., et al. (2024). Trial of lixisenatide in early Parkinson's disease. N. Engl. J. Med. *390*, 1176–1185. https://doi.org/10.1056/NEJMoa2312323.

46. Vijiaratnam, N., Girges, C., Auld, G., McComish, R., King, A., Skene, S.S., Hibbert, S., Wong, A., Melander, S., Gibson, R., et al. (2025). Exenatide once a week versus placebo as a potential disease-modifying treatment for people with Parkinson's disease in the UK: a phase 3, multicentre, double-blind, parallel-group, randomised, placebo-controlled trial. Lancet *405*, 627–636. https://doi.org/10.1016/S0140-6736(24)02808-3.

47. Zhao, L., Li, Z., Vong, J.S.L., Chen, X., Lai, H.-M., Yan, L.Y.C., Huang, J., Sy, S.K.H., Tian, X., Huang, Y., et al. (2020). Pharmacologically reversible zonation-dependent endothelial cell transcriptomic changes with neurodegenerative disease associations in the aged brain. Nat. Commun. *11*, 4413. https://doi.org/10.1038/s41467-020-18249-3.

48. Li, Z., Chen, X., Vong, J.S.L., Zhao, L., Huang, J., Yan, L.Y.C., Ip, B., Wing, Y.K., Lai, H.-M., Mok, V.C.T., et al. (2021). Systemic GLP-1R agonist treatment reverses mouse glial and neurovascular cell transcriptomic aging signatures in a genome-wide manner. Commun. Biol. *4*, 656. https://doi.org/10.1038/s42003-021-02208-9.

49. Cork, S.C., Richards, J.E., Holt, M.K., Gribble, F.M., Reimann, F., and Trapp, S. (2015). Distribution and characterisation of glucagon-like peptide-1 receptor expressing cells in the mouse brain. Mol. Metab. *4*, 718–731. https://doi.org/10.1016/j.molmet.2015.07.008.

50. Fong, H., Zheng, J., and Kurrasch, D. (2023). The structural and functional complexity of the integrative hypothalamus. Science *382*, 388–394. https://doi.org/10.1126/science.adh8488.

51. Schaum, N., Lehallier, B., Hahn, O., Pálovics, R., Hosseinzadeh, S., Lee, S.E., Sit, R., Lee, D.P., Losada, P.M., Zardeneta, M.E., et al. (2020). Ageing hallmarks exhibit organ-specific temporal signatures. Nature *583*, 596–602. https://doi.org/10.1038/s41586-020-2499-y.

52. Olecka, M., van van Bömmel, A., Best, L., Haase, M., Foerste, S., Riege, K., Dost, T., Flor, S., Witte, O.W., Franzenburg, S., et al. (2024). Nonlinear DNA methylation trajectories in aging male mice. Nat. Commun. *15*, 3074. https://doi.org/10.1038/s41467-024-47316-2.

53. Wagner, V., Kern, F., Hahn, O., Schaum, N., Ludwig, N., Fehlmann, T., Engel, A., Henn, D., Rishik, S., Isakova, A., et al. (2024). Characterizing expression changes in noncoding RNAs during aging and heterochronic parabiosis across mouse tissues. Nat. Biotechnol. *42*, 109–118. https://doi.org/10.1038/s41587-023-01751-6.

54. Shoji, H., and Miyakawa, T. (2019). Age-related behavioral changes from young to old age in male mice of a C57BL/6J strain maintained under a

genetic stability program. Neuropsychopharmacol. Rep. *39*, 100–118. https://doi.org/10.1002/npr2.12052.

55. Shoji, H., Takao, K., Hattori, S., and Miyakawa, T. (2016). Age-related changes in behavior in C57BL/6J mice from young adulthood to middle age. Mol. Brain *9*, 11. https://doi.org/10.1186/s13041-016-0191-9.

56. Yanai, S., and Endo, S. (2021). Functional aging in male C57BL/6J mice across the life-span: a systematic behavioral analysis of motor, emotional, and memory function to define an aging phenotype. Front. Aging Neurosci. *13*, 697621. https://doi.org/10.3389/fnagi.2021.697621.

57. Hession, L.E., Sabnis, G.S., Churchill, G.A., and Kumar, V. (2022). A machine-vision-based frailty index for mice. Nat. Aging *2*, 756–766. https://doi.org/10.1038/s43587-022-00266-0.

58. Drucker, D.J. (2022). GLP-1 physiology informs the pharmacotherapy of obesity. Mol. Metab. *57*, 101351. https://doi.org/10.1016/j.molmet.2021.101351.

59. Schmauck-Medina, T., Molière, A., Lautrup, S., Zhang, J., Chlopicki, S., Madsen, H.B., Cao, S., Soendenbroe, C., Mansell, E., Vestergaard, M.B., et al. (2022). New hallmarks of ageing: a 2022 Copenhagen ageing meeting summary. Aging *14*, 6829–6839. https://doi.org/10.18632/aging.204248.

60. López-Otín, C., Blasco, M.A., Partridge, L., Serrano, M., and Kroemer, G. (2023). Hallmarks of aging: An expanding universe. Cell *186*, 243–278. https://doi.org/10.1016/j.cell.2022.11.001.

61. Langfelder, P., and Horvath, S. (2008). WGCNA: an R package for weighted correlation network analysis. BMC Bioinform. *9*, 559. https://doi.org/10.1186/1471-2105-9-559.

62. Arneson, A., Haghani, A., Thompson, M.J., Pellegrini, M., Kwon, S.B., Vu, H., Maciejewski, E., Yao, M., Li, C.Z., Lu, A.T., et al. (2022). A mammalian methylation array for profiling methylation levels at conserved sequences. Nat. Commun. *13*, 783. https://doi.org/10.1038/s41467-022-28355-z.

63. Lu, A.T., Fei, Z., Haghani, A., Robeck, T.R., Zoller, J.A., Li, C.Z., Lowe, R., Yan, Q., Zhang, J., Vu, H., et al. (2023). Universal DNA methylation age across mammalian tissues. Nat. Aging *3*, 1144–1166. https://doi.org/10.1038/s43587-023-00462-6.

64. Zhou, W., Hinoue, T., Barnes, B., Mitchell, O., Iqbal, W., Lee, S.M., Foy, K.K., Lee, K.-H., Moyer, E.J., VanderArk, A., et al. (2022). DNA methylation dynamics and dysregulation delineated by high-throughput profiling in the mouse. Cell Genom. *2*, 100144. https://doi.org/10.1016/j.xgen.2022.100144.

65. Higgins-Chen, A.T., Thrush, K.L., Wang, Y., Minteer, C.J., Kuo, P.-L., Wang, M., Niimi, P., Sturm, G., Lin, J., Moore, A.Z., et al. (2022). A computational solution for bolstering reliability of epigenetic clocks: implications for clinical trials and longitudinal tracking. Nat. Aging *2*, 644–661. https://doi.org/10.1038/s43587-022-00248-2.

66. Bitto, A., Ito, T.K., Pineda, V.V., LeTexier, N.J., Huang, H.Z., Sutlief, E., Tung, H., Vizzini, N., Chen, B., Smith, K., et al. (2016). Transient rapamycin treatment can increase lifespan and healthspan in middle-aged mice. eLife *5*, e16351. https://doi.org/10.7554/eLife.16351.

67. Lamming, D.W., Ye, L., Katajisto, P., Goncalves, M.D., Saitoh, M., Stevens, D.M., Davis, J.G., Salmon, A.B., Richardson, A., Ahima, R.S., et al. (2012). Rapamycin-induced insulin resistance is mediated by mTORC2 loss and uncoupled from longevity. Science *335*, 1638–1643. https://doi.org/10.1126/science.1215135.

68. Ham, D.J., Börsch, A., Chojnowska, K., Lin, S., Leuchtmann, A.B., Ham, A.S., Thürkauf, M., Delezie, J., Furrer, R., Burri, D., et al. (2022). Distinct and additive effects of calorie restriction and rapamycin in aging skeletal muscle. Nat. Commun. *13*, 2025. https://doi.org/10.1038/s41467-022-29714-6.

69. Yin, Z., Guo, X., Qi, Y., Li, P., Liang, S., Xu, X., and Shang, X. (2022). Dietary restriction and rapamycin affect brain aging in mice by attenuating age-related DNA methylation changes. Genes *13*, 699. https://doi.org/10.3390/genes13040699.

70. Xie, K., Fuchs, H., Scifo, E., Liu, D., Aziz, A., Aguilar-Pimentel, J.A., Amarie, O.V., Becker, L., da da Silva-Buttkus, P., Calzada-Wack, J., et al. (2022). Deep phenotyping and lifetime trajectories reveal limited effects of longevity regulators on the aging process in C57BL/6J mice. Nat. Commun. *13*, 6830. https://doi.org/10.1038/s41467-022-34515-y.

71. Keshavarz, M., Xie, K., Schaaf, K., Bano, D., and Ehninger, D. (2023). Targeting the "hallmarks of aging" to slow aging and treat age-related disease: fact or fiction? Mol. Psychiatry *28*, 242–255. https://doi.org/10.1038/s41380-022-01680-x.

72. Péterfi, Z., Szilvásy-Szabó, A., Farkas, E., Ruska, Y., Pyke, C., Knudsen, L.B., and Fekete, C. (2021). Glucagon-like peptide-1 regulates the proopiomelanocortin neurons of the arcuate nucleus both directly and indirectly via presynaptic action. Neuroendocrinology *111*, 986–997. https://doi.org/10.1159/000512806.

73. Secher, A., Jelsing, J., Baquero, A.F., Hecksher-Sørensen, J., Cowley, M.A., Dalbøge, L.S., Hansen, G., Grove, K.L., Pyke, C., Raun, K., et al. (2014). The arcuate nucleus mediates GLP-1 receptor agonist liraglutide-dependent weight loss. J. Clin. Investig. *124*, 4473–4488. https://doi.org/10.1172/JCI75276.

74. Timper, K., del Del Río-Martín, A., Cremer, A.L., Bremser, S., Alber, J., Giavalisco, P., Varela, L., Heilinger, C., Nolte, H., Trifunovic, A., et al. (2020). GLP-1 receptor signaling in astrocytes regulates fatty acid oxidation, mitochondrial integrity, and function. Cell Metab. *31*, 1189–1205.e13. https://doi.org/10.1016/j.cmet.2020.05.001.

75. Folick, A., Cheang, R.T., Valdearcos, M., and Koliwad, S.K. (2022). Metabolic factors in the regulation of hypothalamic innate immune responses in obesity. Exp. Mol. Med. *54*, 393–402. https://doi.org/10.1038/s12276-021-00666-z.

76. Yun, S.P., Kam, T.-I., Panicker, N., Kim, S., Oh, Y., Park, J.-S., Kwon, S.-H., Park, Y.J., Karuppagounder, S.S., Park, H., et al. (2018). Block of A1 astrocyte conversion by microglia is neuroprotective in models of Parkinson's disease. Nat. Med. *24*, 931–938. https://doi.org/10.1038/s41591-018-0051-5.

77. Kopp, K.O., Glotfelty, E.J., Li, Y., and Greig, N.H. (2022). Glucagon-like peptide-1 (GLP-1) receptor agonists and neuroinflammation: Implications for neurodegenerative disease treatment. Pharmacol. Res. *186*, 106550. https://doi.org/10.1016/j.phrs.2022.106550.

78. Gong, N., Xiao, Q., Zhu, B., Zhang, C.-Y., Wang, Y.-C., Fan, H., Ma, A.-N., and Wang, Y.-X. (2014). Activation of spinal glucagon-like peptide-1 receptors specifically suppresses pain hypersensitivity. J. Neurosci. *34*, 5322–5334. https://doi.org/10.1523/JNEUROSCI.4703-13.2014.

79. Wong, C.K., McLean, B.A., Baggio, L.L., Koehler, J.A., Hammoud, R., Rittig, N., Yabut, J.M., Seeley, R.J., Brown, T.J., and Drucker, D.J. (2024). Central glucagon-like peptide 1 receptor activation inhibits Toll-like receptor agonist-induced inflammation. Cell Metab. *36*, 130–143.e5. https://doi.org/10.1016/j.cmet.2023.11.009.

80. Villeda, S.A., Luo, J., Mosher, K.I., Zou, B., Britschgi, M., Bieri, G., Stan, T.M., Fainberg, N., Ding, Z., Eggel, A., et al. (2011). The aging systemic milieu negatively regulates neurogenesis and cognitive function. Nature *477*, 90–94. https://doi.org/10.1038/nature10357.

81. Yousef, H., Czupalla, C.J., Lee, D., Chen, M.B., Burke, A.N., Zera, K.A., Zandstra, J., Berber, E., Lehallier, B., Mathur, V., et al. (2019). Aged blood impairs hippocampal neural precursor activity and activates microglia via brain endothelial cell VCAM1. Nat. Med. *25*, 988–1000. https://doi.org/10.1038/s41591-019-0440-4.

82. Chen, M.B., Yang, A.C., Yousef, H., Lee, D., Chen, W., Schaum, N., Lehallier, B., Quake, S.R., and Wyss-Coray, T. (2020). Brain endothelial cells are exquisite sensors of age-related circulatory cues. Cell Rep. *30*, 4418–4432.e4. https://doi.org/10.1016/j.celrep.2020.03.012.

83. Bieri, G., Schroer, A.B., and Villeda, S.A. (2023). Blood-to-brain communication in aging and rejuvenation. Nat. Neurosci. *26*, 379–393. https://doi.org/10.1038/s41593-022-01238-8.

84. Cai, D., and Khor, S. (2019). "Hypothalamic microinflammation" paradigm in aging and metabolic diseases. Cell Metab. *30*, 19–35. https://doi.org/10.1016/j.cmet.2019.05.021.

85. Zhang, G., Li, J., Purkayastha, S., Tang, Y., Zhang, H., Yin, Y., Li, B., Liu, G., and Cai, D. (2013). Hypothalamic programming of systemic ageing involving IKK-β, NF-κB and GnRH. Nature *497*, 211–216. https://doi.org/10.1038/nature12143.

86. Cota, D., Proulx, K., Smith, K.A.B., Kozma, S.C., Thomas, G., Woods, S.C., and Seeley, R.J. (2006). Hypothalamic mTOR signaling regulates food intake. Science *312*, 927–930. https://doi.org/10.1126/science.1124147.

87. Yang, S.-B., Tien, A.-C., Boddupalli, G., Xu, A.W., Jan, Y.N., and Jan, L.Y. (2012). Rapamycin ameliorates age-dependent obesity associated with increased mTOR signaling in hypothalamic POMC neurons. Neuron *75*, 425–436. https://doi.org/10.1016/j.neuron.2012.03.043.

88. Lee, D.J.W., Kuerec, A.H., and Maier, A.B. (2024). Targeting ageing with rapamycin and its derivatives in humans: a systematic review. Lancet Heal. Longev. *5*, e152–e162. https://doi.org/10.1016/s2666-7568(23)00258-1.

89. Mannick, J.B., Morris, M., Hockey, H.P., Roma, G., Beibel, M., Kulmatycki, K., Watkins, M., Shavlakadze, T., Zhou, W., Quinn, D., et al. (2018). TORC1 inhibition enhances immune function and reduces infections in the elderly. Sci. Transl. Med. *10*, eaaq1564. https://doi.org/10.1126/scitranslmed.aaq1564.

90. Atri, A., Feldman, H.H., Hansen, C.T., Honore, J.B., Johannsen, P., Knop, F.K., Poulsen, P., Raket, L.L., Sano, M., Soininen, H., et al. (2022). evoke and evoke+: design of two large-scale, double-blind, placebo-controlled, phase 3 studies evaluating the neuroprotective effects of semaglutide in early Alzheimer's disease. Alzheimer's Dementia *18*. https://doi.org/10.1002/alz.062415.

91. Kampmann, M. (2024). Molecular and cellular mechanisms of selective vulnerability in neurodegenerative diseases. Nat. Rev. Neurosci. *25*, 351–371. https://doi.org/10.1038/s41583-024-00806-0.

92. van Dyck, C.H., Swanson, C.J., Aisen, P., Bateman, R.J., Chen, C., Gee, M., Kanekiyo, M., Li, D., Reyderman, L., Cohen, S., et al. (2023). Lecanemab in early Alzheimer's disease. N. Engl. J. Med. *388*, 9–21. https://doi.org/10.1056/NEJMoa2212948.

93. Mintun, M.A., Lo, A.C., Duggan Evans, C.D., Wessels, A.M., Ardayfio, P.A., Andersen, S.W., Shcherbinin, S., Sparks, J., Sims, J.R., Brys, M., et al. (2021). Donanemab in early Alzheimer's disease. N. Engl. J. Med. *384*, 1691–1704. https://doi.org/10.1056/NEJMoa2100708.

94. Diallo, A., Carlos-Bolumbu, M., and Galtier, F. (2022). Age, sex, race, BMI, and duration of diabetes differences in cardiovascular outcomes with glucose lowering drugs in type 2 diabetes: A systematic review and meta-analysis. eClinicalMedicine *54*, 101697. https://doi.org/10.1016/j.eclinm.2022.101697.

95. Singh, A.K., and Singh, R. (2020). Gender difference in cardiovascular outcomes with SGLT-2 inhibitors and GLP-1 receptor agonist in type 2 diabetes: A systematic review and meta-analysis of cardio-vascular outcome trials. Diabetes Metab. Syndr. *14*, 181–187. https://doi.org/10.1016/j.dsx.2020.02.012.

96. Pasternak, B., Wintzell, V., Eliasson, B., Svensson, A.-M., Franzén, S., Gudbjörnsdottir, S., Hveem, K., Jonasson, C., Melbye, M., Svanström, H., et al. (2020). Use of glucagon-like peptide 1 receptor agonists and risk of serious renal events: Scandinavian cohort study. Diabetes Care *43*, 1326–1335. https://doi.org/10.2337/dc19-2088.

97. Chang, K., Marran, K., Valentine, A., and Hannon, G.J. (2013). Creating an miR30-based shRNA vector. Cold Spring Harb. Protoc. *2013*, 631–635. https://doi.org/10.1101/pdb.prot075853.

98. Schindelin, J., Arganda-Carreras, I., Frise, E., Kaynig, V., Longair, M., Pietzsch, T., Preibisch, S., Rueden, C., Saalfeld, S., Schmid, B., et al. (2012). Fiji: an open-source platform for biological-image analysis. Nat. Methods *9*, 676–682. https://doi.org/10.1038/nmeth.2019.

99. Gawel, K., Gibula, E., Marszalek-Grabska, M., Filarowska, J., and Kotlinska, J.H. (2019). Assessment of spatial learning and memory in the Barnes maze task in rodents—methodological consideration. Naunyn-Schmiedebergs Arch. Pharmacol. *392*, 1–18. https://doi.org/10.1007/s00210-018-1589-y.

100. Patel, T.P., Gullotti, D.M., Hernandez, P., O'Brien, W.T., Capehart, B.P., Morrison, B., Bass, C., Eberwine, J.E., Abel, T., and Meaney, D.F. (2014). An open-source toolbox for automated phenotyping of mice in behavioral tasks. Front. Behav. Neurosci. *8*, 349. https://doi.org/10.3389/fnbeh.2014.00349.

101. Zhang, C., Li, H., and Han, R. (2020). An open-source video tracking system for mouse locomotor activity analysis. BMC Res. Notes *13*, 48. https://doi.org/10.1186/s13104-020-4916-6.

102. Pence, H.E., and Williams, A. (2010). ChemSpider: an online chemical information resource. J. Chem. Educ. *87*, 1123–1124. https://doi.org/10.1021/ed100697w.

103. Välikangas, T., Suomi, T., and Elo, L.L. (2018). A systematic evaluation of normalization methods in quantitative label-free proteomics. Brief. Bioinform. *19*, 1–11. https://doi.org/10.1093/bib/bbw095.

104. Huber, W., von von Heydebreck, A., Sültmann, H., Poustka, A., and Vingron, M. (2002). Variance stabilization applied to microarray data calibration and to the quantification of differential expression. Bioinformatics *18*, S96–S104. https://doi.org/10.1093/bioinformatics/18.suppl_1.s96.

105. Ritchie, M.E., Phipson, B., Wu, D., Hu, Y., Law, C.W., Shi, W., and Smyth, G.K. (2015). limma powers differential expression analyses for RNA-sequencing and microarray studies. Nucleic Acids Res. *43*, e47. https://doi.org/10.1093/nar/gkv007.

106. Dobin, A., Davis, C.A., Schlesinger, F., Drenkow, J., Zaleski, C., Jha, S., Batut, P., Chaisson, M., and Gingeras, T.R. (2013). STAR: ultrafast universal RNA-seq aligner. Bioinformatics *29*, 15–21. https://doi.org/10.1093/bioinformatics/bts635.

107. Ewels, P., Magnusson, M., Lundin, S., and Käller, M. (2016). MultiQC: summarize analysis results for multiple tools and samples in a single report. Bioinformatics *32*, 3047–3048. https://doi.org/10.1093/bioinformatics/btw354.

108. Anders, S., Pyl, P.T., and Huber, W. (2015). HTSeq—a Python framework to work with high-throughput sequencing data. Bioinformatics *31*, 166–169. https://doi.org/10.1093/bioinformatics/btu638.

109. Love, M.I., Huber, W., and Anders, S. (2014). Moderated estimation of fold change and dispersion for RNA-seq data with DESeq2. Genome Biol. *15*, 550. https://doi.org/10.1186/s13059-014-0550-8.

110. Wu, T., Hu, E., Xu, S., Chen, M., Guo, P., Dai, Z., Feng, T., Zhou, L., Tang, W., Zhan, L., et al. (2021). clusterProfiler 4.0: A universal enrichment tool for interpreting omics data. Innovation *2*, 100141. https://doi.org/10.1016/j.xinn.2021.100141.

111. Gene Ontology Consortium, Aleksander, S.A., Balhoff, J., Carbon, S., Cherry, J.M., Drabkin, H.J., Ebert, D., Feuermann, M., Gaudet, P., Harris, N.L., et al. (2023). The Gene Ontology knowledgebase in 2023. Genetics *224*, iyad031. https://doi.org/10.1093/genetics/iyad031.

112. Kanehisa, M., Furumichi, M., Sato, Y., Kawashima, M., and Ishiguro-Watanabe, M. (2023). KEGG for taxonomy-based analysis of pathways and genomes. Nucleic Acids Res. *51*, D587–D592. https://doi.org/10.1093/nar/gkac963.

113. Bordi, M., Cegli, R.D., Testa, B., Nixon, R.A., Ballabio, A., and Cecconi, F. (2021). A gene toolbox for monitoring autophagy transcription. Cell Death Dis. *12*, 1044. https://doi.org/10.1038/s41419-021-04121-9.

114. Elsasser, S., Elia, L.P., Morimoto, R.I., Powers, E.T., Finley, D., Costa, B., Budron, M., Tokuno, Z., Wang, S., Iyer, R.G., et al. (2023). A comprehensive enumeration of the human proteostasis network. 1. Components of translation, protein folding, and organelle-specific systems. Preprint at bioRxiv. https://doi.org/10.1101/2022.08.30.505920.

115. Elsasser, S., Elia, L.P., Morimoto, R.I., Powers, E.T., Finley, D., Costa, B., Budron, M., Tokuno, Z., Wang, S., Iyer, R.G., et al. (2023). A comprehensive enumeration of the human proteostasis network. 2. Components of the autophagy-lysosome pathway. Preprint at bioRxiv. https://doi.org/10.1101/2023.03.22.533675.

116. Saul, D., Kosinsky, R.L., Atkinson, E.J., Doolittle, M.L., Zhang, X., LeBrasseur, N.K., Pignolo, R.J., Robbins, P.D., Niedernhofer, L.J., Ikeno, Y., et al. (2022). A new gene set identifies senescent cells and

predicts senescence-associated pathways across tissues. Nat. Commun. *13*, 4827. https://doi.org/10.1038/s41467-022-32552-1.

117. Qu, Y., and Ji, Z. (2023). A tissue ubiquitous gene set for cellular senescence. Preprint at bioRxiv. https://doi.org/10.1101/2023.11.21.568150.
118. Schafer, M.J., Zhang, X., Kumar, A., Atkinson, E.J., Zhu, Y., Jachim, S., Mazula, D.L., Brown, A.K., Berning, M., Aversa, Z., et al. (2020). The senescence-associated secretome as an indicator of age and medical risk. JCI Insight *5*, e133668. https://doi.org/10.1172/jci.insight.133668.
119. Tuttle, C.S.L., Luesken, S.W.M., Waaijer, M.E.C., and Maier, A.B. (2021). Senescence in tissue samples of humans with age-related diseases: A systematic review. Ageing Res. Rev. *68*, 101334. https://doi.org/10.1016/j.arr.2021.101334.
120. Gu, C., Shi, X., Dang, X., Chen, J., Chen, C., Chen, Y., Pan, X., and Huang, T. (2020). Identification of common genes and pathways in eight fibrosis diseases. Front. Genet. *11*, 627396. https://doi.org/10.3389/fgene.2020.627396.
121. Wang, B., Chen, S., Qian, H., Chen, R., He, Y., Zhang, X., Xuan, J., Liu, Y., and Shi, G. (2020). Development and validation of a transcriptional signature for the assessment of fibrosis in organs. Preprint at medRxiv. https://doi.org/10.1101/2020.03.14.20024141.
122. Subramanian, A., Tamayo, P., Mootha, V.K., Mukherjee, S., Ebert, B.L., Gillette, M.A., Paulovich, A., Pomeroy, S.L., Golub, T.R., Lander, E.S., et al. (2005). Gene set enrichment analysis: A knowledge-based approach for interpreting genome-wide expression profiles. Proc. Natl. Acad. Sci. USA *102*, 15545–15550. https://doi.org/10.1073/pnas.0506580102.
123. Castanza, A.S., Recla, J.M., Eby, D., Thorvaldsdóttir, H., Bult, C.J., and Mesirov, J.P. (2023). Extending support for mouse data in the Molecular Signatures Database (MSigDB). Nat. Methods *20*, 1619–1620. https://doi.org/10.1038/s41592-023-02014-7.
124. Liberzon, A., Birger, C., Thorvaldsdóttir, H., Ghandi, M., Mesirov, J.P., and Tamayo, P. (2015). The Molecular Signatures Database hallmark gene set collection. Cell Syst. *1*, 417–425. https://doi.org/10.1016/j.cels.2015.12.004.
125. Howe, D.G., Blake, J.A., Bradford, Y.M., Bult, C.J., Calvi, B.R., Engel, S.R., Kadin, J.A., Kaufman, T.C., Kishore, R., Laulederkind, S.J.F., et al. (2018). Model organism data evolving in support of translational medicine. Lab Anim. *47*, 277–289. https://doi.org/10.1038/s41684-018-0150-4.
126. Gu, Z., and Hübschmann, D. (2023). simplifyEnrichment: a Bioconductor package for clustering and visualizing functional enrichment results. Genom. Proteom. Bioinform. *21*, 190–202. https://doi.org/10.1016/j.gpb.2022.04.008.
127. Zhou, W., Triche, T.J.J., Laird, P.W., and Shen, H. (2018). SeSAMe: reducing artifactual detection of DNA methylation by Infinium BeadChips in genomic deletions. Nucleic Acids Res. *46*, e123. https://doi.org/10.1093/nar/gky691.
128. Ding, W., Kaur, D., Horvath, S., and Zhou, W. (2023). Comparative epigenome analysis using Infinium DNA methylation BeadChips. Brief. Bioinform. *24*, bbac617. https://doi.org/10.1093/bib/bbac617.

CellPress
OPEN ACCESS

STAR★METHODS

KEY RESOURCES TABLE

REAGENT or RESOURCE	SOURCE	IDENTIFIER
Antibodies		
Anti-GLP-1R antibody	Abcam, UK	ab218532; RRID: AB_2864762
Goat anti-rabbit IgG-Alexa Fluor 568 conjugate	Invitrogen, US	A-11011; RRID: AB_143157
Chemicals, peptides, recombinant proteins		
Exendin-4	MedChem Express, China	HY-13443
Rapamycin	MedChem Express, China	HY-10219
TRIzol reagent	Thermo Fisher Scientific, US	15596018
RNAlater	Thermo Fisher Scientific, US	AM7021
RNA/DNA shield	Zymo Research, US	R1200-125
Tissue-Tek Optimal Cutting Temperature (O.C.T.) compound	Sakura Finetek, US	4583
Critical commercial assays		
RNAqueous kit	Thermo Fisher Scientific, US	AM1912
Quick-DNA Miniprep Plus Kit	Zymo Research, US	D4069
E.Z.N.A. Tissue DNA Kit	Omega Bio-Tek, US	D3396-02
Deposited data		
Raw and pre-processed RNA sequencing data	This study	SRA: PRJNA1177532; GEO: GSE280382
Raw and pre-processed DNA methylation data	This study	GEO: GSE279437
Values used to create all graphs in the paper	This study	Data S1
Experimental models: Organisms/strains		
C57BL/6 mice	Laboratory Animal Service Center of CUHK	N/A
C57BL/6J mice	Jackson Laboratory	000664
Oligonucleotides		
Short hairpin RNA (shRNA) for *Glp1r* knockdown (sequence: 5′-GCGTCAACTTTCTTATCTTCA-3′)	BrainVTA(Wuhan), China	N/A
Scrambled shRNA (sequence: 5′-CCTAAGGT TAAGTCGCCCTCG-3′)	BrainVTA(Wuhan), China	N/A
AAV-2/9 encoding shRNAs	BrainVTA(Wuhan), China	N/A
Software and algorithms		
MATLAB	MathWorks, US	R2022a & R2023a
MouseActivity	https://github.com/HanLab-OSU/MouseActivity	N/A
Autotyping toolbox	https://www.seas.upenn.edu/~molneuro/software.html	v15.04
Fiji ImageJ	https://imagej.net/software/fiji/downloads	v1.54p
R	The R Project for Statistical Computing, https://www.r-project.org/	v4.2.2 & v.4.3.1
STAR	https://github.com/alexdobin/STAR/releases/tag/2.7.10b	v2.7.10b
Mus musculus genome assembly	Ensembl	GRCm39
FastQC	https://github.com/s-andrews/FastQC/releases/tag/v0.11.9	v0.11.9
MultiQC	https://github.com/MultiQC/MultiQC	v1.13a
HTSeq	https://htseq.readthedocs.io/en/master/index.html	v2.0.2
DESeq2	https://bioconductor.org/packages/release/bioc/html/DESeq2.html	v1.38.3
WGCNA	https://cran.r-project.org/web/packages/WGCNA/index.html	v1.72-5
clusterProfiler	https://guangchuangyu.github.io/software/clusterProfiler/	v4.4.4 & v4.6.2

(*Continued on next page*)

Continued

REAGENT or RESOURCE	SOURCE	IDENTIFIER
simplifyEnrichment	https://www.bioconductor.org/packages/release/bioc/html/simplifyEnrichment.html	v1.12.0
SeSAMe	https://www.bioconductor.org/packages/release/bioc/html/sesame.html	v1.16.1
dnaMethyAge	https://github.com/yiluyucheng/dnaMethyAge/tree/main	v0.2.0
Other		
Grip strength meter	Shanghai Xin-Ruan Instruments Inc., China	XR501
Accelerated rotarod test equipment	Shanghai Xin-Ruan Instruments Inc., China	R03-1
Barnes maze	This study (custom-built)	N/A
Open field arena	This study (custom-built)	N/A
Camera	Logitech, China	StreamCam
Waters ACQUITY UPLC BEH C18 column (1.7 μm, 2.1 mm × 100 mm)	Waters, US	186002350
BGI metabolome database	BGI Genomics Inc.	N/A
mzCloud database	https://www.mzcloud.org/	N/A
ChemSpider database	https://www.chemspider.com/	N/A
Gene Ontology database	https://geneontology.org/	N/A
KEGG database	https://www.genome.jp/kegg/pathway.html	N/A
Custom array consisting of Infinium Mouse Methylation BeadChip (mm285k) and Mammalian methylation (mm40k) arrays	Clock Foundation	N/A

EXPERIMENTAL MODEL AND SUBJECT DETAILS

Experimental Animals

All experimental procedures were approved in advance by the Animal Experimentation Ethics Committee of the Chinese University of Hong Kong (CUHK), and were carried out in accordance with the Guide for the Care and Use of Laboratory Animals. All C57BL/6 mice were bred and provided by the Laboratory Animal Service Center of CUHK unless otherwise specified, and maintained at controlled temperature (22–23 °C) with an alternating 12-hour light/dark cycle with free access to standard mouse diet and water. The ambient humidity was maintained at < 70 % relative humidity.

Three cohorts of male mice were used. For the aging/aged long-term treatment cohort, mice were treated with the GLP-1RA exendin-4 (a.k.a. exenatide) or vehicle from 11 months old (m.o.) for 30 weeks (see next section for details of drug and vehicle treatments). A group of 3 m.o. mice that received vehicle treatment for 4 weeks were included as a control group. For the young long-term treatment cohort, mice were treated with exendin-4 or vehicle from 3 m.o. for 26 weeks. For the aged short-term treatment cohort, mice were imported from the Jackson Laboratory. 17 m.o. aged mice received adeno-associated virus (AAV) vector-mediated hypothalamic *Glp1r* knockdown or a control AAV injection (see below for details). They were allowed to recover from AAV injection for 4 weeks, and subsequently subjected to vehicle, exendin-4 or rapamycin treatment from 18 m.o. for 13 weeks. A control group of young mice (4 m.o.) underwent a control AAV injection and 4 weeks recovery period, and then received vehicle treatment from 5 m.o. for 7 weeks. Details of animal cohort sizes are specified in Table S1. Sample sizes for each functional test and molecular readout in different tissue organs are indicated in the respective plots.

METHOD DETAILS

Exendin-4 and rapamycin treatment

Exendin-4 (HY-13443, MedChem Express, China) was reconstituted in phosphate-buffered saline (PBS) to 1 mg/ml and further diluted in PBS to 4.2 μg/ml. For all GLP-1RA treatment groups, each mouse received daily intraperitoneal (i.p.) injections of exendin-4 at a dosage of 21 μg/kg body weight (bw) (equivalent to 5 nmol/kg bw/day). Rapamycin (HY-10219, MedChem Express, China) was dissolved in absolute ethanol to 10 mg/ml and subsequently diluted in a vehicle solution consisting of 5% Tween 80, 5% PEG-400, and PBS to 0.8 mg/ml. For the mTOR inhibitor treatment group, each mouse received i.p. injections of rapamycin at a dosage of 8 mg/kg bw on alternate days (equivalent to 8.75 μmol/kg bw/2 days). Mice in the vehicle control groups received daily volume-matched i.p. PBS injections.

CellPress
OPEN ACCESS

AAV-mediated hypothalamic Glp1r knockdown

Short hairpin RNA (shRNA) (sequence: 5'-GCGTCAACTTTCTTATCTTCA-3') for *Glp1r* knockdown was constructed into the miR-30 scaffold[97] driven by the EF1a promoter, and packaged into recombinant AAV-2/9. Control AAV contained a scrambled sequence (5'-CCTAAGGTTAAGTCGCCCTCG-3'). Young (4 m.o.) and aged (16 m.o.) mice were anesthetized by i.p. injection of 150 mg/kg bw ketamine and 10 mg/kg bw xylazine, and positioned in a stereotaxic frame (Model 68528, RWD Life Science, China) for injection. A total of 1 microliter AAV (containing 5–6 $\times$ 10^9 vg) was injected into the hypothalamus of each mouse. To ensure a broad regional coverage of the hypothalamus, AAVs were delivered to four sites, with coordinates as follows: anteroposterior (AP) = -1.6 mm, mediolateral (ML) = ±0.25 mm, dorsoventral (DV) = -5.9 mm from the dura (0.2 μl per site), and AP = -2 mm, ML = ±0.25 mm, DV = -5.85 mm from the dura (0.3 μl per site), covering bilateral hypothalamus. To verify *Glp1r* transcript knockdown efficiency with quantitative PCR, brains were removed after PBS perfusion and half of the dissected hypothalamus tissues from 3 mice per experimental group were used for RNA extraction using TRIzol reagent (15596018, Thermo Fisher Scientific, US). Primers used for transcript amplification were: *Glp1r* (forward: 5'-CAGTGGGGTACGCACTTTCT-3'; reverse: 5'-TAACGAACAGCAGCGGAACT-3'); *Gapdh* (forward: 5'-CATCTTCCAGGAGCGAGACC-3'; reverse: 5'-GGCGGAGATGATGACCCTTT-3').

Immunohistochemistry for validation of *Glp1r*/GLP-1R knockdown

An additional cohort of mice underwent identical *Glp1r*/GLP-1R knockdown procedure with bilateral hypothalamic *Glp1r* shRNA or scramble shRNA AAV injections. Mice were euthanized and underwent transcardial perfusion with 20 mL of ice-cold PBS, followed by 10 mL of 4% paraformaldehyde (PFA). The brains were extracted from the cranium, post-fixed in 4% PFA overnight, and subsequently dehydrated using 30% sucrose. After being embedded into the Tissue-Tek Optimal Cutting Temperature (O.C.T.) compound (4583, Sakura Finetek, US), the brains were sectioned into 40 μm slices. The brain sections were treated with 30% formic acid for 10 minutes for antigen retrieval, 0.5% Triton X-100 for 10 minutes for tissue permeabilization, and blocked with 5% normal goat serum in PBS for one hour. The sections were then incubated with 2 μg/mL anti-GLP-1R antibody (ab218532, Abcam, UK) in the blocking buffer containing 0.1% Triton X-100, at room temperature for one hour, followed by washing for three times in 0.3% Triton X-100/PBS, and incubated with 2 μg/mL goat anti-rabbit IgG-Alexa Fluor 568 conjugate (A-11011, Invitrogen, US) at room temperature for one hour.

Confocal imaging was performed using a Leica TCS SP8 confocal microscope. Excitation wavelength was 552 nm and detection was done with the passband set to 557 to 789 nm, using a HC PL FLUOTAR L $\times$20/0.40 CORR PH1 dry objective. For each set of images in Figures S7A and S7B, and in Figures S7C and S7D, brain slices were processed and stained in the same batch, and identical imaging parameters were applied. Each image for a given field of view under the objective was acquired as the average of three images, and image tiles were automatically stitched together using built-in functions of the confocal microscope control software. Each set of 8-bit TIFF output images were subjected to identical processing in Fiji ImageJ[98] (v1.54p), which included manual cropping, median filtering with the radius input parameter set to 0.5, as well as simple image contrast and brightness adjustment by setting the pixel intensity range to the same range ([32, 192] for all images in Figures S7A and S7B, and [8, 192] for those in Figures S7C and S7D).

Forelimb grip strength test

A grip strength meter (Model XR501, Shanghai Xin-Ruan Instruments Inc., Shanghai, China) was used to measure forelimb grip strength. The mouse subject was allowed to grip the mesh lattice with its forelimbs. The peak force to pull the mouse away from the grip was recorded. For each mouse, the average value from five repeated measurements was obtained, with 15-minute intervals between successive measurements.

Accelerated rotarod test

The accelerated rotarod test equipment (Model R03-1, Xin-Ruan Instruments Inc., Shanghai, China) consisted of a 3-cm diameter rod. Mice were trained to habituate to the rotating rod by walking on it at a low constant speed (4 rotations per minute (R.P.M.), 2 min $\times$ 3 sessions with 15-min intervals at the baseline, and 2 min $\times$ 1 session at the 3- or 6-month treatment time points). During testing, rod rotation was linearly accelerated from 4 to 40 R.P.M over 5 minutes. The endpoint was reached when the mouse could not withstand the rotation and fell from the rod, or resisted falling over 5 minutes. For each mouse, the average duration to reach the endpoint in five trials was obtained, with 15-minute intervals between successive trials.

Barnes maze

A home-made Barnes maze was used, which consisted of a white acrylic round disk (90-cm diameter) with 20 holes (5-cm diameter) radially evenly spaced at 5 cm from the outer edge. 19 of the 20 holes were blocked while the remaining one provided access to an escape box (i.e., the target). Visual cues were placed around the maze in the testing room. On the first day, mice were first trained to find the escape box. At the beginning of the assay, the mouse subject was covered by a cardboard box at the center of the maze. Five seconds later, an aversive noise was initiated from a nearby device (900 Hz, 80 dB), and the box was removed to permit exploration and escape. Entering the escape box was defined as a successful escape event. Mice that failed to find the escape box in 3 minutes were guided to it using a glass cylinder. On assay day one, a one-hour interval after initial training was included before testing was conducted once. From assay days two to four, the aging/aged long-term treatment cohort and corresponding young adult controls were tested twice daily with a one-hour interval between trials, and the two measurements were averaged to obtain daily

performance measures. For the young adult long-term treatment cohort, mice were tested once daily throughout the four assay days. For the aging/aged long-term treatment cohort, probe trials were conducted 24 hours after the last acquisition trial.[99] These lasted for 3 minutes each and were carried out using the same experimental setup without the escape route (i.e., all holes were blocked).

Performance was quantified using primary latency (i.e., time to first reach and explore the correct target for > 0.5 second) and error count (i.e., number of wrong holes explored before first reaching the correct target) for acquisition trials on assay days 1 to 4, and proportion of time spent in the target quadrant in probe trials, through video analysis by adapting the Autotyping toolbox[100] (v15.04) in MATLAB R2023a (MathWorks, US). For the aging/aged long-term treatment cohort, animals were excluded from primary latency analysis on specific days due to video timestamp corruption or animals going out of the maze. Exclusions were as follows: day 1, 1 young adult control; day 2, 1 aged exenatide-treated animal; day 4, 1 aged vehicle-treated animal. The final number of data points included was 109 (out of 112). Animals were also excluded from error count analysis due to suboptimal camera placement that resulted in small parts of non-target holes being out of view, or the animal going out of view during testing. Exclusions were as follows: day 1, 1 aged exenatide-treated animal, 3 young adult controls; day 2, 1 aged exenatide-treated animal, 2 young adult controls; day 3, 1 young adult control; and day 4, 1 aged vehicle-treated animal. The final number of data points included was 103 (out of 112). These were accounted for in statistical tests (see below section on statistics). All videos were manually inspected individually to verify the extracted measures.

Open-field test and frailty index

The open-field test was performed in a home-made 56 cm × 56 cm arena with opaque walls. The mouse was placed in the arena and allowed to freely explore for 10 minutes, while its locomotion was recorded from above using a camera (StreamCam, Logitech, China). The total distance traveled and proportion of time spent in the center (defined as the squared area within center 2/3 of each dimension) vs. periphery (outside the center) were extracted from the video using the open-source package MouseActivity[101] in MATLAB R2022a (MathWorks, US). We adapted a machine vision-based algorithm for frailty analysis based on the open-field test data.[57] In brief, the video recordings were processed by pre-trained models[57] to extract features of the mouse including coordinates, pose, gait, and grooming behavior. Behavioral features in individual frames were then processed with custom scripts to produce feature summaries for each video. Frailty index (FI) score predictions were then generated from pre-trained linear mixed models (based on the FI score dataset of the original study[57]) and the features summaries. To ensure comparability, data entries measured in count, duration, and displacement were divided by the respective recording's total duration to transform into ratios, and all data entries were normalized and scaled by its own population mean and standard deviation, following the protocol adopted in the original study.[57]

Y-maze

A custom-made Y-maze consisting of 3 arms (each with dimensions of 30-cm length, 8-cm width, and 15-cm height) and a center area (27.7 cm^2) was used. During the training phase, mice were allowed to explore the Y-maze for 5 minutes with one arm (arm 2) closed off. Two minutes later, the previously closed arm was released and the animals were reintroduced from another arm (arm 3) into the maze to freely explore for 5 minutes. The mouse exploratory behavior was recorded by a camera (StreamCam, Logitech, China) and the video recordings were processed using a custom script written in MATLAB R2022a (MathWorks, US), using background subtraction and blob detection to extract the head coordinates and orientation. Exploration of a given arm was defined as when the head and the whole body trunk of the animal were inside the arm area. Percentage of time spent in the novel arm was calculated by dividing the time exploring arm 2 by the sum of time the animal spent in all three arms.

Statistical tests for physical and cognitive tests

To evaluate the longitudinal aging effects, one-sided Page's trend test was applied to the raw values of the forelimb grip strength, rotarod and Y-maze performance measures to examine the presence of any significant decline with age in these parameters. To evaluate longitudinal treatment effects on forelimb grip strength, rotarod and Y-maze performance, the corresponding measurements relative to vehicle control group for each mouse were calculated by subtracting the values at the corresponding time points by the corresponding group mean values of vehicle-treated mice. One-sided Page's trend test was used to examine the presence of any significant increase across time observed in the treatment group. The performance of animal subjects in the Barnes maze across treatment groups over the four assay days was analyzed using two-way repeated measures ANOVA (if no missing data) or two-way mixed ANOVA (to account for presence of missing data). Comparisons of locomotor activity level and proportion of time spent at periphery between the vehicle- and exendin-4-treated groups were conducted using two-sided rank-sum tests. Comparisons of FI across age groups were conducted using one-way ANOVA with Tukey's HSD post-hoc test for multiple comparisons. Treatment effects on FI in both aged and young cohorts were conducted using two-sided rank-sum tests. Differences in forelimb grip strength, rotarod, and Y-maze performances between groups at baseline and after 6 months of treatment were evaluated using one-sided rank-sum tests (to examine if exenatide group > vehicle group values). Linear model fitting on the treatment group performance measures (after subtracting vehicle group means) incorporating for each animal both their body weight changes from baseline and time effects, and examination of the correlations between behavioral performance measures changes in body weight from baseline were performed.

Metabolic assessment

The body weight of each mouse was monitored on a weekly basis. The mice in each treatment group were housed together in a single cage. The food provided to each cage was weighed once weekly and averaged to determine the daily food intake per mouse. For the long-term (30- and 26-week) treatment experiments, the monitoring started at baseline (one week before starting treatment) and continued until the conclusion of the study. For the short-term (13-week) treatment experiment, it began at baseline and was conducted for seven weeks following the initiation of treatment. The impact of treatments on longitudinal body weight was assessed using two-way repeated-measures ANOVA.

Drug or vehicle administration was halted on the day of fasting blood glucose measurement or oral glucose tolerance test (OGTT). Mice underwent a 6-hour fasting period prior to fasting blood glucose measurement or OGTT. For OGTT, blood glucose levels were measured from tail vein samples at the baseline, and then at 15, 30, 60, and 120 minutes after administration of 2 g/kg bw of glucose via oral gavage. Comparison of fasting blood glucose levels in the vehicle- vs. exendin-4-treated groups, and at baseline vs. after 6-month treatment, was conducted using two-way repeated measures ANOVA. Area under the curve (AUC) values were calculated from the measurements obtained from OGTT, and compared across experimental groups using one-way ANOVA with Holm-Sidak's post-hoc multiple comparisons test.

Statistical software for assessing physical, behavioral, and metabolic readouts

Behavioral and metabolic data were plotted and visualized with custom scripts in Python (v3.12.7). Page's trend tests for forelimb grip strength, rotarod and Y-maze performance measures were carried out using the scipy.stats.page_trend_test function of the SciPy package (v1.15.2). Comparisons of raw values of behavioral readouts at baseline and 6 months of treatment were carried out using the scipy.stats.mannwhitneyu function of the SciPy package (v1.15.2) with exact *P*-values calculation. One-way ANOVA with post hoc Tukey's HSD tests and rank-sum test for comparing FI across ages or treatment groups were performed using the scipy.stats.f_oneway function of SciPy (v1.15.2), the statsmodels.stats.multicomp.pairwise_tukeyhsd function of statsmodels (v0.14.2), and the scipy.stats.mannwhitneyu function (with exact *P*-value) of SciPy (v1.15.2), respectively. Linear model fitting for behavioral performance measures with respect to time (treatment duration) and change in body weight from baseline was performed using the ols function of the statsmodels package (v0.14.2), along with statistical significance assessment for the fitted coefficients. The correlations between change in body weight from baseline and behavioral performance measures were determined using the scipy.stats.pearsonr function of the SciPy package (v1.15.2) and the sklearn.linear_model.LinearRegression class of the scikit-learn package (v1.5.1). Comparisons of open-field locomotor activity and time spent in periphery, as well as gonadal fat as percentage of body weight across two treatment groups (Figures 1L and 1X), were also carried out using the scipy.stats.mannwhitneyu function (with exact *P*-value) of SciPy (v1.15.2). Other statistical comparisons of Barnes maze performance measures, fasting blood glucose, OGTT, longitudinal body weight changes, and gonadal fat as percentage of body weight (Figure S8D) were carried out in GraphPad Prism (v8.0.2). Data are presented as mean ± standard error of mean (S.E.M.) or standard deviation (S.D.), or median with interquartile range, as indicated at appropriate places.

Tissue collection and storage

On the day of tissue collection, mice received the final dose of vehicle or drug treatment in the morning, followed by a 6-hour fasting period. Mice were euthanized via isoflurane inhalation and transcardially perfused with 20 ml of ice-cold PBS. Mouse brains were removed from the cranium and underwent further manual microdissection to isolate the hypothalamus, hippocampus, and frontal cortex bilaterally. From the heart, the left ventricle was collected for RNA extraction, and the left atrium for DNA extraction. The quadriceps femoris muscle was collected as the skeletal muscle sample. For the colon, the proximal segment was collected. The whole liver, spleen, bilateral kidneys and lungs were dissected and parts of the tissue were collected. Bilateral gonadal adipose tissues were collected, and weighed prior to further processing (aging/aged long-term treatment cohort: $n = 3$ and 6 mice had the adipose tissues weighted for vehicle control and exenatide-treated groups respectively; for all other cohorts, adipose tissue weighting was done for all animal subjects). The collected tissues from different organs were further dissected into smaller pieces, each with largest dimension < 5 mm and preserved in RNAlater (AM7021, Thermo Fisher Scientific, US) for RNA extraction, or RNA/DNA shield (R1200-125, Zymo Research, US) for DNA extraction. All samples were stored at -20°C before extraction.

The blood samples were lysed in an ice-cold red blood cell lysis buffer for 20 minutes. The white blood cells were separated via centrifugation at 500 ×g, 4°C for 10 minutes, and subsequently lysed into TRIzol reagent (15596018, Thermo Fisher Scientific, US) for future RNA extraction, or genomic DNA lysis buffer (BioFluid & Cell Buffer, Zymo Research, US) for DNA extraction. Plasma was isolated from EDTA-anticoagulated blood samples by centrifugation at 1,600 ×g, 4°C for 15 minutes. The samples were stored at -80°C before RNA / DNA extraction or further assays.

Total RNA and genomic DNA extraction

The tissues were retrieved from RNAlater (AM7021, Thermo Fisher Scientific, US), combined with the TRIzol reagent (15596018, Thermo Fisher Scientific, US) or the lysis buffer of the RNAqueous kit (AM1912, Thermo Fisher Scientific, US), homogenized using the TissueLyser II system (Qiagen, US), and total RNA extraction was performed following the instructions in the vendor's manuals. Genomic DNA was extracted using a similar procedure, with blood DNA extracted with the Quick-DNA Miniprep Plus Kit (D4069, Zymo Research, US) and solid tissue DNA extracted using the E.Z.N.A. Tissue DNA Kit (D3396-02, Omega Bio-Tek, US).

RNA sequencing

Total RNA samples were sent for library preparation and sequencing by Novogene (Novogene Biology Information Technology Co., Ltd., Beijing, China). Quality control including sample quantitation, integrity and purity were assessed by Novogene using Nanodrop and Agilent 5400 fragment analyzer systems. Samples with an RNA integrity number above 4 were kept for analysis. Libraries were prepared with a poly(A) selection strategy using the NEBNext Ultra II RNA Library Prep Kit for Illumina (E7770, New England Biolabs, US). Sequencing was carried out on an Illumina NovaSeq 6000 (150 base pairs paired end) for all samples.

Plasma metabolomic measurement

Plasma metabolomic profiling was performed using high-throughput liquid chromatography-mass spectrometry (LC-MS) at BGI Genomics Inc. (Shenzhen, China). To extract metabolites, 100 μl of plasma from each mouse was combined with 700 μl of extractant containing internal standard (methanol:acetonitrile:water = 4:2:1, v/v/v), shaken for 1 minutes and kept at -20°C for 2 hours. The samples were then centrifuged at 25,000 ×g, 4°C for 15 minutes. The supernatant was collected and the solvent was dried out. The pellet was subsequently reconstituted in 180 μl of methanol:water (1:1 v/v) and the sample was centrifuged again at 25,000 ×g, 4°C for 15 minutes. The resulting supernatant was subjected to LC-MS/MS analysis, using the Waters UPLC I-Class Plus equipped with a Waters ACQUITY UPLC BEH C18 column (1.7 μm, 2.1 mm × 100 mm) (Waters, US) and tandem Q-Exactive high resolution mass spectrometer (Thermo Fisher Scientific, US). Pooled plasma reference samples, which were prepared by combining small aliquots from the study samples, were analyzed among the participant samples to monitor the repeatability of the analysis process.

The column temperature was maintained at 45°C. The mobile phase consisted of 0.1% formic acid (A) and acetonitrile (B) in the positive mode, and in the negative mode, the mobile phase consisted of 10 mM ammonium formate (A) and acetonitrile (B). The gradient conditions were as follows: 0–1 min, 2% B; 1–9 minutes, 2%–98% B; 9–12 minutes, 98% B; 12–12.1 minutes, 98% B to 2% B; and 12.1–15 minutes, 2% B. The flow rate was 0.35 ml/min and the injection volume was 5 μl. The full scan range was 70–1050 m/z with a resolution of 70000, and the automatic gain control (AGC) target for MS acquisitions was set to 3×10^6 with a maximum ion injection time of 100 ms. Top 3 precursors were selected for subsequent MS-MS fragmentation with a maximum ion injection time of 50 ms and resolution of 17500, with the AGC set at 1×10^5. The stepped normalized collision energy was set to 20, 40 and 60 eV. ESI parameter settings were: sheath gas flow rate 40, aux gas flow rate 10, positive-ion mode spray voltage (|KV|) 3.80, negative-ion mode spray voltage (|KV|) 3.20, capillary temperature 320°C, aux gas heater temperature 350°C.

Bioinformatic data analysis

All analysis was performed with R (v4.2.2) unless otherwise specified.

Metabolome data analysis

The mass spectrometry data were processed by BGI Genomics Inc. (Shenzhen, China) using the Compound DiscoverTM 3.3 software (Thermo Fisher Scientific, US) and analyzed in combination with the BGI metabolome, mzCloud, and ChemSpider[102] online databases. A data matrix containing information, including metabolite identification and peak area was obtained for further analysis.

The normalized intensities further underwent variance-stabilizing transformation to account for systematic bias.[103,104] After mean variance stabilization, differential analysis was performed using linear models as implemented within the limma package[105] (v3.54.2) in R. Spearman correlation coefficients (R_S) and *P*-values were calculated by correlating the log fold changes per metabolite in aged drug-treated vs. aged vehicle-treated mice and in aged vehicle-treated vs. young vehicle-treated mice.

RNA-sequencing data analysis

Raw sequencing FASTQ files were mapped with STAR[106] (v2.7.10b) with default parameters using the *Mus musculus* genome assembly GRCm39. Quality control was carried out with the FastQC (v0.11.9) and MultiQC[107] (v1.13a) packages. HTSeq[108] (v2.0.2) was used to obtain read counts with default options except 'mode' being set to 'intersection-strict', and 'nonunique' being set to 'fraction' for ambiguous reads. Gene counts were filtered for a minimum of at least 10 reads in a minimum number of samples, with the minimum number based on the number of animals constituting the smallest comparator group size in the experiment.

Downstream analysis was done with custom scripts in R (v4.2.2 and v4.3.1). Read counts were normalized with DESeq2 vst for exploratory data analysis and heatmap visualizations. Differential expression analysis was performed with DESeq2[109] (v1.38.3). Log fold change estimates were shrunken with the approximate posterior estimate for generalized linear models method. Significant differentially expressed genes (DEGs) were taken as those with a false discovery rate (FDR)-adjusted *P*-value < 0.05. We grouped the DEGs into six categories according to their pattern of differential expression by comparing DEGs in five combinations of contrasts, namely 1) aged GLP-1RA-treated vs. aged vehicle-treated mice against aged vehicle-treated vs. young vehicle-treated mice, 2) the same comparison but with hypothalamic *Glp1r* knockdown, 3) aged GLP-1RA-treated vs. aged vehicle-treated mice against aged mTORi-treated vs. aged vehicle-treated mice, 4) young GLP-1RA-treated vs. young vehicle-treated mice against aged GLP-1RA-treated vs. aged vehicle-treated mice, and 5) aged GLP-1RA-treated vs. aged vehicle-treated mice (with hypothalamic *Glp1r* KD) against aged GLP-1RA-treated vs. aged vehicle-treated mice (with hypothalamic scramble shRNA AAV injection).

For the first two contrasts, the DEGs were labeled "counteraction" where the GLP1-RA treatment-associated change and the age-associated change were in the opposite direction, or "exacerbation" where the GLP-1RA treatment-associated change was in the same direction as the age-associated change. An additional label of "Rx-dominant" was given for where only the GLP-1RA treatment-associated change reached statistical significance, and of "aging-dominant" was given for where only the age-associated

change reached statistical change. No additional label was given if both comparisons were significant. The top 50 protein-coding genes counteracted by exenatide (Figures 2 and S2) were defined by first ranking the absolute value of the product of log2 fold changes in aging and with exenatide treatment for all "counteraction" protein-coding DEGs, then selecting the top 25 exenatide-upregulated, and top 25 downregulated genes. For the third comparison, the patterns were labeled "same" where the GLP-1RA treatment-associated change and mTORi treatment-associated change were in the same direction, and "opposite" when the changes were in the opposite direction. We further specified the dominant agent depending on which treatment yielded the statistically significant change. No additional label was given if both comparisons were significant. For the fourth comparison, the patterns were labeled "same" where the GLP-1RA treatment-associated changes in young and in aged mice were in the same direction, and "opposite" when the changes were in the opposite direction. We further specified the dominant effect depending on which age group treatment yielded the statistically significant change. No additional label was given if both comparisons were significant. For the fifth comparison, the patterns were labeled "same" where the GLP-1RA treatment-associated changes in aged mice with hypothalamic *Glp1r* KD and scramble shRNA AAV injection were in the same direction, and "opposite" when the changes were in the opposite direction. We further specified the dominant effect group depending on which comparison yielded the statistically significant change. No additional label was given if both were significant. R_S and *P*-values for each contrast were calculated by correlating the log fold changes per gene in the pair of comparisons.

Principal component analysis (PCA)

DESeq2 vst-normalized counts were taken for PCA with the base R prcomp function. All genes were used for analysis. Centroids for each group were plotted using the mean value of the plotted principal components of each treatment group.

Weighted gene co-expression network analysis

WGCNA[61] (v1.72-5) was conducted with the DESeq2 vst-normalized count matrix. For each tissue type, a signed-hybrid network was constructed with biweight midcorrelation, with the soft threshold chosen dynamically for each tissue at the level at which the scale-free topology model fit reached 0.8. The minimum module size was set at 30. Module eigengenes (i.e., module first principal components) were used to summarize modules, and modules with eigengene correlation > 0.7 were merged.

Differential eigengene analysis was performed by comparing the eigengene expressions of each sample across comparator groups with a Wilcoxon rank-sum test or a Kruskal-Wallis test. An FDR of < 0.1 was taken to denote a significant difference in module eigengene expression across experimental groups. In each set of analysis, the differentially expressed gene modules were categorized based on one or both experimental comparisons reaching FDR-adjusted statistical significance level (i.e., Figures 3E and 5E: aging, exenatide treatment, or both; Figure 6H: exenatide, rapamycin, or both treatments), and the directionality of change if both comparisons attained significance (for Figures 3E and 5E only: counteraction or exacerbation).

Pathway enrichment analysis

Pathway enrichment was done with clusterProfiler[110] (v4.4.4) against the Gene Ontology[111] and KEGG[112] databases, custom gene sets of functional pathways related to aging curated from the literature,[113–121] and the Molecular Signatures Database (MSigDB)[122–124] (HALLMARK_INFLAMMATORY_RESPONSE,[125] WP_INFLAMMATORY_RESPONSE_PATHWAY, WP_LUNG_FIBROSIS, WP_IMMUNE_INFILTRATION_IN_PANCREATIC_CANCER). For each tissue, all genes that underwent differential expression analysis were used as the background gene set.

In pathway enrichment analyses for DEGs, "counteraction" DEGs (significant for at least one comparison) were used (clusterProfiler v4.4.4 enrichGO). To assist in pathway enrichment analysis interpretability, enriched terms from the comparisons were visualized using the simplifyEnrichment package[126] (simplifyGOFromMultipleLists) (v1.12.0).

For gene modules from WGCNA, the genes with a correlation of > 0.7 with the module eigengene were used as input in custom enrichment analysis (clusterProfiler v4.6.2 enricher).

DNA methylation analysis

DNA methylation assays were carried out by the Clock Foundation using a custom BeadChip array containing loci from the Infinium Mouse Methylation BeadChip (i.e., mm285k array[64]) and the mammalian methylation array (i.e., mm40k array[62]). Data analysis was performed with SeSAMe[127,128] (v1.16.1). In brief, raw IDAT files were read with the Sesame prepSesameData function, with the SHCDPB masks (inferSpecies, prefixMaskButC, inferInfiniumIChannel, dyeBiasNL, pOOBAH, noob). This retained 279,644 probes from the mm285k array for downstream analysis. Differential methylation testing per locus was performed with the normalized β values using mixed linear models as implemented in the Sesame package via the DML function. To analyze methylation sites based on the mm40k array, we obtained an imputed β-value data matrix provided by the Clock Foundation, containing 36,793 probes. We then similarly ran the differential analysis.

The differentially methylated loci (DML, nominal *P*-value < 0.05) were categorized based on the differential pattern across various combinations of contrasts, namely 1) aged GLP-1RA-treated vs. aged vehicle-treated mice against aged vehicle-treated vs. young vehicle-treated mice, 2) the same comparison but with hypothalamic *Glp1r* knockdown, 3) aged GLP-1RA-treated vs. aged vehicle-treated mice against aged mTORi-treated vs. aged vehicle-treated mice, and 4) aged GLP-1RA-treated vs. aged vehicle-treated mice (with hypothalamic *Glp1r* KD) against aged GLP-1RA-treated vs. aged vehicle-treated mice (with hypothalamic scramble shRNA AAV injection).

For the first two contrasts, the DMLs were labeled ''counteraction'' where the GLP1-RA treatment-associated change and the age-associated change were in the opposite direction, or ''exacerbation'' where the GLP-1RA treatment-associated change was in the same direction as the age-associated change. An additional label of ''Rx-dominant'' was given for where only the GLP-1RA treatment associated change reached statistical significance, and of ''aging-dominant'' was given for where only the age-associated change reached statistical change. No additional label was given if both comparisons were significant. For the third comparison, the patterns were labeled ''same'' where the GLP-1RA treatment-associated change and mTORi treatment-associated change were in the same direction, and ''opposite'' when the changes were in the opposite direction. We further specified the dominant agent depending on which treatment yielded the statistically significant change. No additional label was given if both comparisons were significant. For the fourth comparison, the patterns were labeled ''same'' where the GLP-1RA treatment-associated changes in aged mice with hypothalamic *Glp1r* KD and scramble shRNA AAV injection were in the same direction, and ''opposite'' when the changes were in the opposite direction. We further specified the dominant effect group depending on which comparison yielded the statistically significant change. No additional label was given if both were significant. R_S and *P*-values for each contrast were calculated by correlating the delta β value (Δβ) per locus in the pair of comparisons.

Epigenetic age clock analysis

Two epigenetic clocks were selected for analysis, a universal clock,[63] and one re-trained with a principal components computational solution to enhance robustness.[65] Both clocks were accessed and calculated via the dnaMethyAge package (v0.2.0). For inputs, a Clock Foundation imputed version of the custom BeadChip array results (with ∼40k features as per the original mammalian methylation array[62]) was used. This was run through the methyAge function, with species set as *Mus musculus*. Outputs were compared across experimental groups with Kruskal-Wallis tests with post-hoc Dunn's tests.

Permutation sensitivity analysis

We performed permutation sensitivity analyses to assess the robustness of (*i*) the molecular age-counteracting effects of exenatide and rapamycin, and (*ii*) the similarities of molecular effects of exenatide and rapamycin in aged mice, covering all applicable transcriptomic and DNAm datasets. For (*i*), this was conducted by shuffling aged sample experimental group labels with respect to treatment (i.e., vehicle or drug) for the data of each tissue organ (without shuffling the young adult group), while keeping the sample number constant for each group, and calculating the so-obtained R_S with shuffling for 5,000 (transcriptome data) or 1000 (methylome data) times, or the maximum number of combinations where sample numbers were limiting. For (*ii*), sample group label shuffling was carried out for the vehicle and exenatide groups (without shuffling the rapamycin group) for the maximum number of combinations. The shuffling procedure disrupts only the potential treatment effects of exenatide and rapamycin for (*i*), and of exenatide for (*ii*), while preserving all other statistical aspects of the data. The distribution of R_S from the permutation analysis was then compared against the number of treatment label mismatches induced by the shuffling for each tissue organ from aged animals. The number of differential features (genes or methylation loci) was also compared against the number of mismatches induced by the shuffling.